AD-A285 077

‖‖‖‖‖‖‖‖‖‖‖‖‖‖‖

# Application of Fourier-Space Image-Restoration Techniques to Turbulence Compensation and Sparse-Aperture Imaging

R.R. Parenti

1 June 1994

## Lincoln Laboratory

MASSACHUSETTS INSTITUTE OF TECHNOLOGY

*LEXINGTON, MASSACHUSETTS*

DTIC QUALITY

94-31046

‖‖‖‖‖‖‖‖‖‖‖‖‖

'94 9

MASSACHUSETTS INSTITUTE OF TECHNOLOGY
LINCOLN LABORATORY

# APPLICATION OF FOURIER-SPACE IMAGE-RESTORATION TECHNIQUES TO TURBULENCE COMPENSATION AND SPARSE-APERTURE IMAGING

*R.R. PARENTI*
*Group 94*

Accesion For

| NTIS    CRA&I | X |
| DTIC    TAB | ☐ |
| Unannounced | ☐ |
| Justification |  |

By

Distribution /

Availability Codes

| Dist | Avail and/or Special |

*A-1*

**TECHNICAL REPORT 996**

**1 JUNE 1994**

DTIC QUALITY INSPECTED 3

LEXINGTON                    MASSACHUSETTS

# EXECUTIVE SUMMARY

## OVERVIEW OF DECONVOLUTION METHODS

This investigation was motivated by the success of speckle interferometry, which was first proposed by Labeyrie [1] in 1970 as a means of achieving partial correction for the degrading effects of atmospheric turbulence. Using this relatively simple computational procedure, in which spatial-frequency information from an ensemble of images is combined with a statistical description of the turbulence power spectrum, astronomers have been able to obtain near-diffraction-limited autocorrelation functions of celestial objects. Knowledge of the autocorrelation function is particularly useful when studying systems having a relatively simple composition, such as binary stars [2,3,4].

Speckle interferometry is a subset of a reconstruction technique known as deconvolution, which was first applied by Nathan [5] to improve images received from the early Ranger and Mariner missions. An estimate of the undistorted image, $I$, is obtained from the distorted image, $I'$, through a Fourier domain multiplicative operation that makes use of a priori knowledge of the sensor's optical transfer function ($OTF$)

$$I \approx \mathcal{F}^{-1}\left\{\left\langle\frac{\mathcal{F}\{I'\}}{OTF}\right\rangle\right\} .$$

This process effectively deconvolves the camera's point spread function from the recorded data. Perfect results are obtained in the limit of infinite signal-to-noise (S/N), as long as the $OTF$ is non-zero out to the band limit of the receiver. Under finite noise conditions it can be shown that a Wiener deconvolution filter incorporating a minimum mean-square estimator produces an optimal reconstruction [6].

Descriptions of data-recovery techniques designed to ameliorate the effects of temporally and spatially invariant blurring can be found in a number of standard texts [7,8]. Nonstationary processes can generally be handled using a similar mathematical formalism; however, in this case a more detailed characterization of the pupil-plane transfer function is required to achieve good performance.

This report investigates two practical applications of the Fourier deconvolution process. The first deals with the correction of atmospheric turbulence effects that are encountered by ground-based optical telescopes. The second application demonstrates the feasibility of recovering near-diffraction-limited images from a lightweight space telescope, incorporating a sparse-aperture construction.

## APPLICATION OF DECONVOLUTION TO TURBULENCE COMPENSATION

Adaptive optics for atmospheric turbulence compensation has been an active area of research within the military community for over two decades [9,10], and more recently, these concepts have also been successfully applied in the field of astronomy [11]. The traditional approach to this problem involves the use of a phase sensor, which measures the wavefront of the electric field in the aperture plane of the system, and a deformable mirror, which applies the conjugate phase. Turbulence is an example of a physical process that is nonstationary in both space and time; to achieve good correction at visible wavelengths it may be necessary to actuate the mirror at several hundred positions at an update rate in excess of 1 kHz.

For applications involving imaging (as opposed to beam propagation), aberrations introduced by the atmosphere can be reduced by using a time-dependent system transfer function to perform a real-time deconvolution of the image information. The advantage of this approach, as compared with a full adaptive-optics system, is that an active control element is not required to eliminate turbulence-induced phase distortions. Section 3 of this report compares the performance characteristics of these two alternatives using experimental data obtained as part of the Laboratory's Short Wavelength Adaptive Techniques (SWAT) program [12]. The analysis shows that deconvolution can produce an image that is comparable to that obtainable with a full adaptive-optics system, but a much longer dwell time is usually required to achieve the same level of performance.

## APPLICATION OF DECONVOLUTION TO SPARSE-APERTURE IMAGING

*Sparse-aperture telescopes* are highly advantageous in situations where the costs associated with the deployment of a normal receiver would be prohibitive. Under ideal conditions all the mirror segments would be stationary and have the same phase, in which case the optical transfer function is real and time-independent. This imaging geometry would appear to be well suited for image deconvolution techniques, and Section 4 addresses the relevant performance issues.

As an aid in this part of the investigation, a three-petal telescope structure having a 10% fill factor is used as a model to study the reconstruction process and its sensitivity to sensor noise. It is demonstrated that a receiver of this type can produce pictures that are comparable to those generated by a filled aperture of the same diameter, provided that an average signal-to-noise ratio of 10 can be maintained over the entire image. The results of this study are very promising and lend strong support to the feasibility of constructing inexpensive, lightweight surveillance satellites employing folded-mirror architecture.

# ACKNOWLEDGMENTS

# TABLE OF CONTENTS

# LIST OF ILLUSTRATIONS

# LIST OF ILLUSTRATIONS (Continued)

# LIST OF ILLUSTRATIONS (Continued)

# LIST OF TABLES

# 1. INTRODUCTION

Image reconstruction is important in any application in which the sensing apparatus or the intervening medium significantly corrupts the recorded data. Deconvolution processes are the oldest and best understood [5,6], although alternative methods involving nonlinear and iterative computational methods can provide better performance when real-time data processing is not a requirement [13,14,15,16,17]. For many practical problems, however, Fourier domain deconvolution is the method of choice, because acceptable results can usually be obtained with a minimum of computational effort.

Speckle interferometry is an example of a deconvolution process that uses statistical information about the atmosphere to form an estimate of the effective modulation transfer function (*MTF*) that is stationary in space and time [4]. This technique has been successfully applied in the field of astronomy for over 20 years, but until recently it has not been possible to obtain a two-dimensional time-dependent description of the aperture-plane wavefront. A solution to this problem has been developed by investigators within the adaptive optics community, who have fielded a number of devices for wavefront characterization [9,10]. Furthermore, the use of laser guide stars has recently been demonstrated [12,18,19] and can be used to generate a bright turbulence probe in situations where the object body is unable to supply sufficient light for this purpose. The motivation exists, therefore, to take a fresh look at the process of combining aperture- and image-plane data.

This report describes two practical applications of the Fourier-deconvolution process in which detailed knowledge of the system's instantaneous optical transfer function (*OTF*) is effectively utilized. In the first example, speckle imagery is combined with wavefront-sensor data to produce diffraction-limited images of celestial objects; the results are shown to compare favorably with the output of a fully operational adaptive optics system. The second application involves a sparse-aperture collection system that could be incorporated into a lightweight space telescope; this discussion includes an assessment of the practical utility of sparse-aperture receivers in a realistic S/N environment.

1

# 2. OVERVIEW OF DECONVOLUTION METHODS

Although the first known use of Fourier deconvolution predates its application in speckle interferometry by several years, for the purpose of this report it will be instructive to discuss the basic deconvolution concepts as they relate to the reconstruction of astronomical images that have been corrupted by atmospheric turbulence. Of particular interest is the evolution from techniques that employ a statistical description of the atmospheric *OTF* to methods that incorporate detailed characterizations that are resolved in both space and time. A review of the basic principles governing the formation of a focal-plane image in the presence of turbulence is provided in the Appendix.

## 2.1 SPECKLE INTERFEROMETRY

In 1970 Labeyrie [1] proposed a way to process an ensemble of short-exposure images to obtain a diffraction-limited autocorrelation function. This technique is based on the observation that an image-plane speckle pattern can be thought of as a kind of multiple-exposure picture containing many complete representations of the original object. Since a spatial displacement in real space corresponds to a phase shift in Fourier space, the phase-invariant properties of the object can be extracted through a fairly simple transformation. This process is now described.

The original implementation of speckle interferometry involved the use of photographic plates that were exposed for short periods so that the individual turbulence realizations could be frozen during the exposure time; see Figure 1. The intensity function, $I'$, recorded by each plate is related to the object function, $I$, in the following manner:

$$I' = I \otimes PSF_c \otimes PSF_t \ , \tag{1}$$

where $PSF_c$ is the point spread function for the diffraction-limited system and $PSF_t$ is the instantaneous point spread function due to turbulence. In the next step, each plate is illuminated by a collimated monochromatic beam that forms an image referred to as a "specklegram" in the Fourier plane. The intensity distribution of a single specklegram is equal to the square of the Fourier transform of the speckle pattern

$$|\mathcal{F}\{I'\}|^2 = |\mathcal{F}\{I\}|^2 \ MTF_c^2 \ MTF_t^2 \ , \tag{2}$$

where $MTF_c$ and $MTF_t$ represent the modulation transfer functions of the aperture and short exposure turbulence, respectively. When the same specklegram plate is exposed to a number of speckle images in this manner, the ensemble average is formed:

$$\langle |\mathcal{F}\{I'\}|^2 \rangle = |\mathcal{F}\{I\}|^2 \ MTF_c^2 \ \langle MTF_t^2 \rangle \ . \tag{3}$$

3

SPECKLE IMAGE       "SPECKLEGRAM"

230550-1

AUTOCORRELATION FUNCTION
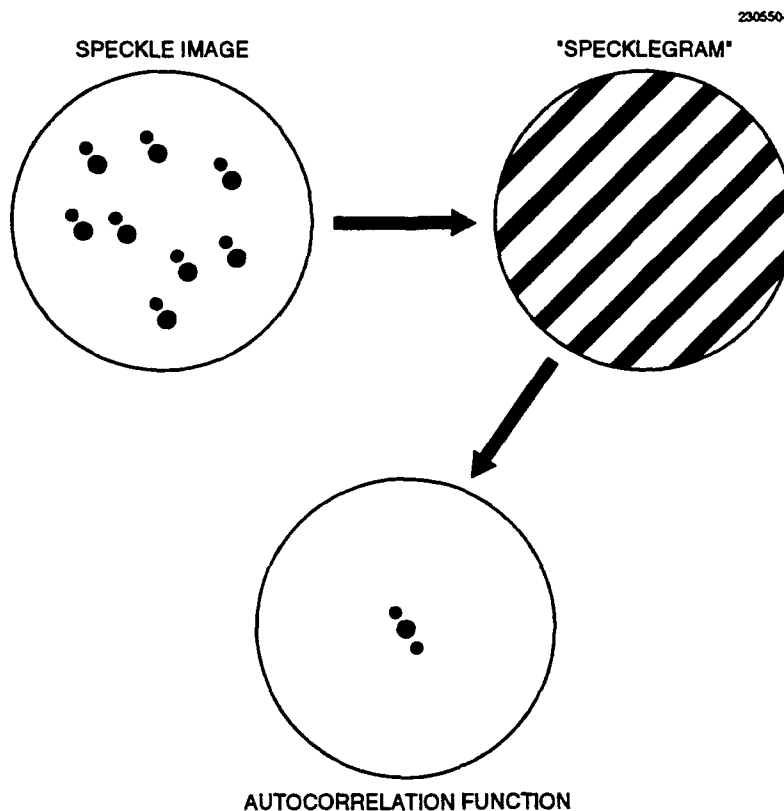
*Figure 1. Processing steps used to generate a diffraction-limited autocorrelation function from an ensemble of speckle images. In the original version of this process, the specklegram was formed optically using Fourier transform optics.*

For isotropic turbulence, the time-averaged *MTF* will have circular symmetry, and its shape will be governed principally by the turbulence coherence length, $r_o$. If the statistical properties of the atmosphere change slowly with time, the data ensemble can be made as large as necessary to achieve the desired signal-to-noise ratio. Furthermore, an independent measurement of $\langle MTF_t^2 \rangle$ can be obtained by imaging a bright star in the neighborhood of the object under investigation.

To justify the final step of the restoration process, observe that the diffraction-limited autocorrelation function of a point source is the Fourier transform of the square of the aperture *MTF*

$$\mathcal{R}_c = \mathcal{F}^{-1}\left\{ MTF_c^2 \right\} \quad , \tag{4}$$

4

and the diffraction-limited autocorrelation function of the object intensity distribution is

$$\mathcal{R}_I = \mathcal{F}^{-1}\left\{ |\mathcal{F}\{I\}|^2 \ MTF_c^2 \right\} \ .$$ (5)

When this result is combined with Equation (3) it can be seen that

$$\mathcal{R}_I = \mathcal{F}^{-1}\left\{ \frac{\left\langle |\mathcal{F}\{I'\}|^2 \right\rangle}{\left\langle MTF_t^2 \right\rangle} \right\} \ .$$ (6)

The numerator of the transform operand is the specklegram defined in Equation (3). To accomplish this operation the specklegram plate is digitized, divided by an estimate of $\left\langle MTF_t^2 \right\rangle$, and the transform of the resulting ratio is then computed numerically. With modern cameras and computational equipment it is far more convenient to digitize each realization of $I'$ and perform all subsequent summation and Fourier transform operations on a real-time digital computer.

An important caveat is added here regarding the reconstruction of images corrupted by atmospheric turbulence. As indicated earlier, the high spatial-frequency structure of turbulence tends to break up the focal-plane image into an array of speckles, each containing a diffraction-limited replica of the object. Unfortunately, the scale of this pattern is proportional to wavelength so that if broadband light having a bandwidth of $\Delta\lambda$ is used to form the image, the individual speckles will be smeared by an average angle of $\Delta\lambda/r_o$ in the radial direction. Because the width of the diffraction-limited point spread function is $\lambda/D$ for an aperture of diameter $D$, good restoration results can be achieved only if $(\Delta\lambda/\lambda)<(r_o/D)$. For this reason astronomers typically use a fractional bandwidth of the order of 5% when performing speckle interferometry with large telescopes.

Equation (6) provides a template for all the processing techniques that are discussed in the remainder of this report. As indicated in Figure 2, the transfer function of a nonideal system generally attenuates the high spatial-frequency components of the scene. But for frequencies below the cutoff point, the original OTF can be restored through an appropriate renormalization process in the Fourier domain. In principle, this type of operation can always be performed as long as the pupil function is accurately known.

5
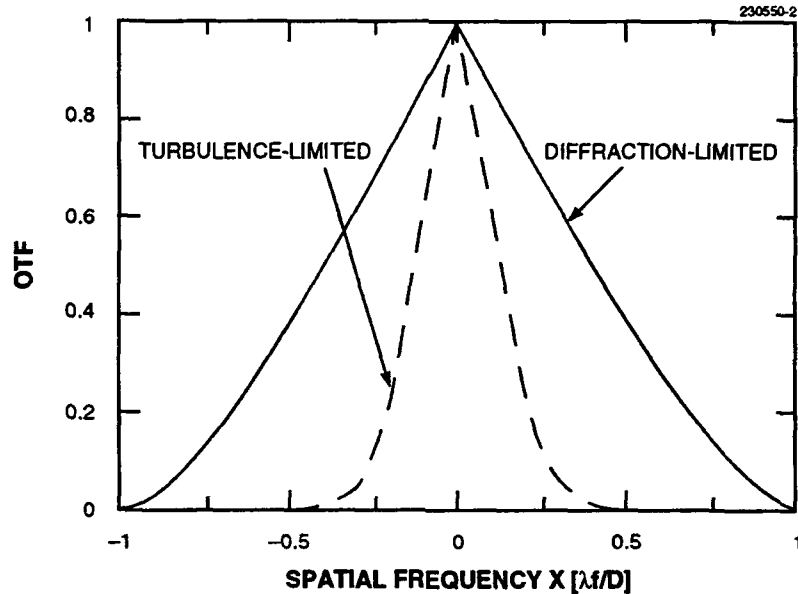
*Figure 2.* Comparison of receiver transfer functions for diffraction-limited viewing and with the addition of atmospheric turbulence.

## 2.2 IMAGE RECONSTRUCTION WITH WAVEFRONT SENSING

Although speckle interferometry has provided astronomers with a powerful tool to overcome the effects of atmospheric turbulence, the final output is not an uncorrupted image of an astronomical object, but rather its autocorrelation function. Such information is sufficient for objects having a simple geometry, such as a binary star, but of limited use for more complex bodies. The key to extracting true imagery is to somehow estimate the instantaneous *OTF* as opposed to its time-averaged modulus. A variety of computational methods for extracting the transfer function's phase information have been published [20,21,22], and an excellent overview of work performed at Lincoln Laboratory has recently appeared in *The Lincoln Laboratory Journal* [23].

Astronomers are just beginning to make use of crude wavefront sensors to aid in the control of large mirror segments and have attempted to combine the principles of speckle interferometry with phase sensor data. Such an approach has been proposed by Rousset, Primot, and Fontanella [24,25], who assume that the instantaneous aperture-plane turbulence wavefront, $t_S$, is recorded along with each speckle image; from this information the turbulence *OTF* can be computed:

$$OTF_t = \left[ t_s \otimes t_s^* \right] . \tag{7}$$

6

When this information is combined with the far-field data, the following estimate of the diffraction-limited image can be made:

$$\tilde{I} = \mathcal{F}^{-1}\left\{ \left\langle \frac{\mathcal{F}\{I'\}}{OTF_t} \right\rangle \right\} \ , \tag{8}$$

where it is essential that aperture- and image-plane data are simultaneously recorded for each turbulence realization in the ensemble.

The practical implementation of Equation (8) requires a few minor adjustments to avoid difficult numerical calculations and mathematical singularities. Note that knowledge of the turbulence function is limited to the aperture region; the measurable quantities are the aperture *OTF* and the total *OTF*:

$$OTF_c = \left[ P \otimes P^* \right] \quad \text{and} \quad OTF = \left[ (Pt_s) \otimes (Pt_s)^* \right] \ , \tag{9}$$

where *P* represents the pupil function. Since it is also desirable to avoid division by a complex function, the following form is found to be convenient:

$$\tilde{I} = \mathcal{F}^{-1}\left\{ \left\langle \frac{MTF_c \, OTF^* \, \mathcal{F}\{I'\}}{MTF^2} \right\rangle \right\} \approx \mathcal{F}^{-1}\left\{ \frac{MTF_c}{\langle MTF^2 \rangle} \left\langle OTF^* \, \mathcal{F}\{I'\} \right\rangle \right\} \ , \tag{8.a}$$

where the factoring of the expectation value is possible because the *MTF* of the diffraction-limited aperture is not time dependent, and the turbulence *MTF* varies only slowly with time. The final consideration relates to the magnitude of the composite function that multiplies $\mathcal{F}\{I'\}$ in the operand of the last equation. At high spatial frequencies this number may exceed the signal-to-noise ratio by several orders of magnitude, which can result in an output image that is completely noise dominated. The simplest correction involves the insertion of a constant in the denominator

$$\tilde{I} \approx \mathcal{F}^{-1}\left\{ \frac{MTF_c}{\langle MTF^2 \rangle + \varepsilon} \left\langle OTF^* \, \mathcal{F}\{I'\} \right\rangle \right\} \ , \tag{8.b}$$

where the value of $\varepsilon$ must be carefully chosen to maximize the degree of restoration without significantly increasing the root-mean-square noise. Equation (8.b) represents the general form of the Fourier-deconvolution operator as applied in this report. A method for constructing an optimized, frequency-dependent expression for $\varepsilon$ is developed next.

7

## 2.3 OPTIMAL RECONSTRUCTION OF IMAGES WITH ADDITIVE NOISE

The fundamental flaw in the technique just outlined is that restoration of the midrange frequencies will also enhance the noise within that spectral region. Fortunately, this flaw is not fatal to the concept as long as suitable modifications are introduced.

The general problem can be treated as one of optimal estimation in which one wishes to reproduce a given signal as accurately as possible in the presence of additive noise. The signal in this case is defined as the noise-free image produced by a circular aperture of diameter $D$,

$$I_c = I \otimes PSF_c \quad . \tag{10}$$

The actual image formed by the system contains two principal components: the first derives from the convolution of the pupil point spread function, the turbulence point spread function, and the object function; the second is represented by an additive noise contribution, $n(x,y)$. In the data processing step the sensor output is convolved with a two-dimensional operator, $g(x,y)$, which is optimized to recover the diffraction-limited image

$$\tilde{I} = g \otimes \left\{ I \otimes PSF_c \otimes PSF_t + n \right\} = g \otimes \left\{ I' + n \right\} \quad . \tag{11}$$

To achieve optimal performance, $g$ is formulated so that the error function

$$e = \left\langle \left( I_c - \tilde{I} \right)^2 \right\rangle \tag{12}$$

is minimized over some two-dimensional region.

Problems similar to those presented in Equation (12) have been treated previously [6,8,26], but the inclusion of two different point spread functions introduces a complication that requires a somewhat more general approach. To simplify the notation it is assumed for the moment that the signal is a function of the single spatial variable, $x$. For a noncausal filter, the squared error at position $x$ is equal to

$$e^2(x) = I_c^2(x) - 2I_c(x)\tilde{I}(x) + \tilde{I}^2(x) \quad . \tag{13}$$

It was assumed in Equation (11) that the best estimate of the image is

$$\tilde{I}(x) = g(x) \otimes \left\{ I'(x) + n(x) \right\} = \int g(u) \left\{ I'(x-u) + n(x-u) \right\} dx \quad . \tag{14}$$

The expectation value of the squared error can be written

$$\left\langle e^2(x) \right\rangle = \Re_c(0) - 2\int g(u)\, \Re_{c,I+n}(u)\, du + \int\int g(u)\, g(v)\, \Re_{I+n}(u-v)\, du\, dv \quad , \tag{15}$$

where the integration associated with the expectation operator has been performed first to produce a set of correlation functions, which are represented in this expression by the variable $\Re$. The parameter $\Re_c$ is the autocorrelation of the diffraction-limited output, $\Re_{t+n}$ is the autocorrelation of the sum of the telescope's output signal and the associated noise, and $\Re_{c,t+n}$ is the cross-correlation function. Because the noise is assumed to be uncorrelated with the input signal, the cross-correlation function in the second term can be replaced with $\Re_{c,t}$ so that

$$\left\langle e^2(x) \right\rangle = \Re_c(0) - 2\int g(u)\, \Re_{c,t}(u)\, du + \iint g(u)\, g(v)\, \Re_{t+n}(u-v)\, du\, dv \quad . \tag{15.a}$$

Differentiating with respect to $g(u)$ for all values of $u$ gives the optimization condition

$$\int g(u)\, \Re_{t+n}(x-u)\, du = \Re_{c,t}(x) \quad , \tag{16}$$

where the left side is recognized as a convolution operation. The Fourier transform of this expression yields the result

$$G(s) = \frac{\mathcal{F}\{I_c(x)\}\, \mathcal{F}^*\{I'(x)\}}{\left|\mathcal{F}\{I'(x)+n(x)\}\right|^2} = \frac{\mathcal{F}\{I_c(x)\}\, \mathcal{F}^*\{I'(x)\}}{\left|\mathcal{F}\{I'(x)\}\right|^2 + \left|\mathcal{F}\{n(x)\}\right|^2} \quad . \tag{17}$$

Equation (17) represents the operator with an output that most nearly matches the noise-free image formed by the diffraction-limited aperture. Combining this result with the Fourier transforms of Equations (10) and (11) gives a complete description of the transformation

$$\tilde{I} = \mathcal{F}^{-1}\left\{\left\langle \frac{MTF_c\ OTF^*\ \mathcal{F}\{I'+n\}}{MTF^2 + F_n/F_o} \right\rangle\right\} \approx \mathcal{F}^{-1}\left\{ \frac{MTF_c}{\left\langle MTF^2 \right\rangle + F_n/F_o} \left\langle OTF^*\ \mathcal{F}\{I'+n\}\right\rangle \right\} \quad , \tag{18}$$

where $F_o = \left|\mathcal{F}\{I\}\right|^2$ and $F_n = \left|\mathcal{F}\{n\}\right|^2$ are the power spectral density functions associated with the object and the system noise, respectively. If the uncorrupted image is unresolved by the receiver (as would be the case for an isolated star) and the noise is assumed to have no spatial structure, then $F_n/F_o$ will be a constant equal to the square of the signal-to-noise ratio of the optical power. The appropriate form for more complex scenes is developed in Section 4.

9

# 3. THE APPLICATION OF FOURIER-DECONVOLUTION TECHNIQUES TO TURBULENCE COMPENSATION

At visible wavelengths the earth's atmosphere severely limits the ability of ground-based telescopes to form clear images of celestial objects. The physical effect, which is referred to as "atmospheric turbulence," is the result of thermally induced changes in the air's index of refraction. Light that passes through a turbulent medium experiences random and spatially nonuniform variations of phase across its wavefront. As described in Section A-2, the effective resolution of a terrestrial telescope is limited by the turbulence coherence length, $r_o$, which is typically of the order of 20 cm under good seeing conditions.

The introduction of speckle interferometry in the early '70s [1] represents the first attempt by the astronomical community to ameliorate the effects of atmospheric turbulence. As indicated earlier in Section 2, however, this technique can only be used to extract the object's autocorrelation function. To form real images, some means must be found to accurately measure the wavefront phase in the pupil plane of the telescope. Wavefront sensors capable of performing this type of measurement have been developed by researchers in the field of adaptive optics [9,11].

Two methods of turbulence compensation are currently available to the astronomer. The first is accomplished through the use of a complete adaptive-optics system that incorporates a mechanical device, known as a deformable mirror, to remove any phase distortions present in the pupil plane. In the second approach, phase measurements are computationally combined with the uncorrected focal-plane imagery using the techniques described previously. This section addresses the hardware implementation of these two concepts and provides a comparison of performance using data collected in two star-imaging experiments.

## 3.1 HARDWARE IMPLEMENTATION

An adaptive-optics system can be thought of as a highly parallel servo device that simultaneously nulls the phase fluctuations of the incoming wavefront at many discrete locations over a two-dimensional field; see Figure 3. Phase errors are sensed by the wavefront sensor, which transmits control signals to the deformable mirror. To achieve good performance, the high spatial-frequency correction must be updated at approximately 1 kHz by a mirror having an actuator spacing that is somewhat smaller than the turbulence coherence length. An excellent description of the theory and operation of a state-of-the-art adaptive-optics system can be found in the spring 1992 edition of *The Lincoln Laboratory Journal* [10,12].

A computational image-reconstruction system based on the application of Equation (18) requires both the focal-plane image and knowledge of the system's instantaneous *OTF* and is accomplished using the system design shown in Figure 4. A comparison of Figures 3 and 4 shows than in the latter design the deformable mirror has been replaced by a computer that combines the near-field and far-field data to provide a prediction of the image that would have been seen in the absence of turbulence.

11

The data-reconstruction approach just described is potentially advantageous in reducing overall system cost and complexity. The relative performance of these approaches in both high and low S/N conditions is now addressed.
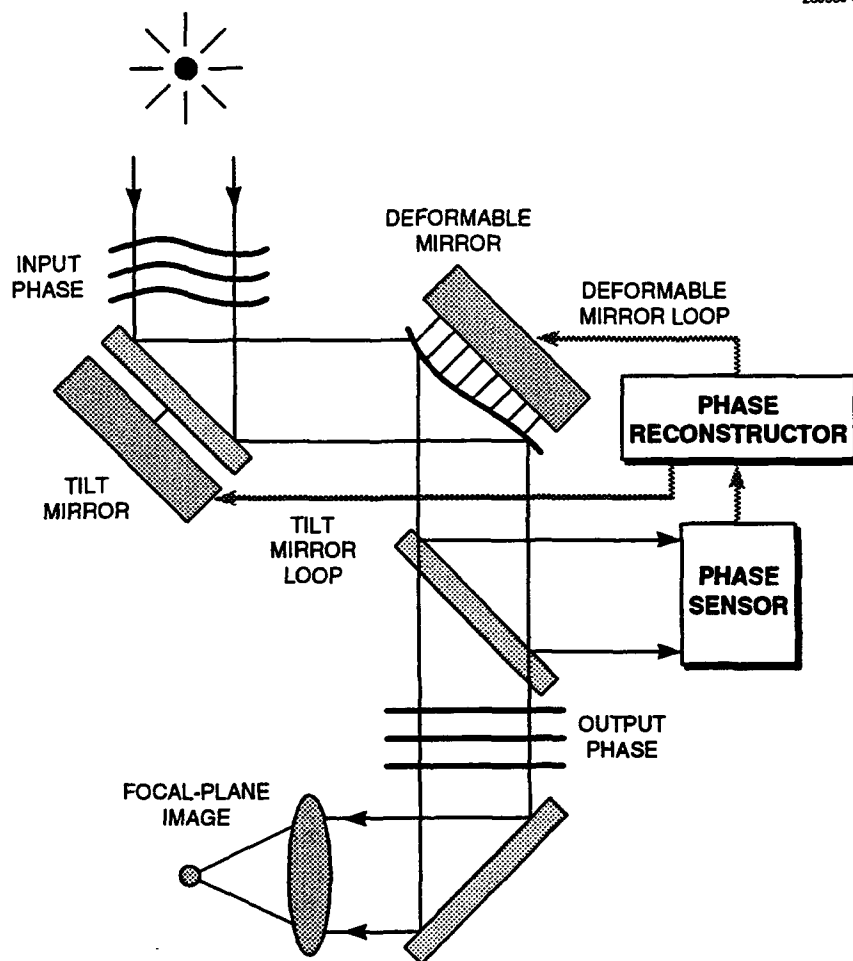
*Figure 3. Essential components of an adaptive-optics, phase-compensation system. The first derivative of the phase difference between the incoming wavefront and the surface figure imposed by the tilt and deformable mirrors is measured by the phase sensor. Residual phase error is computed by the reconstructor and subsequently applied to the two active optical elements.*
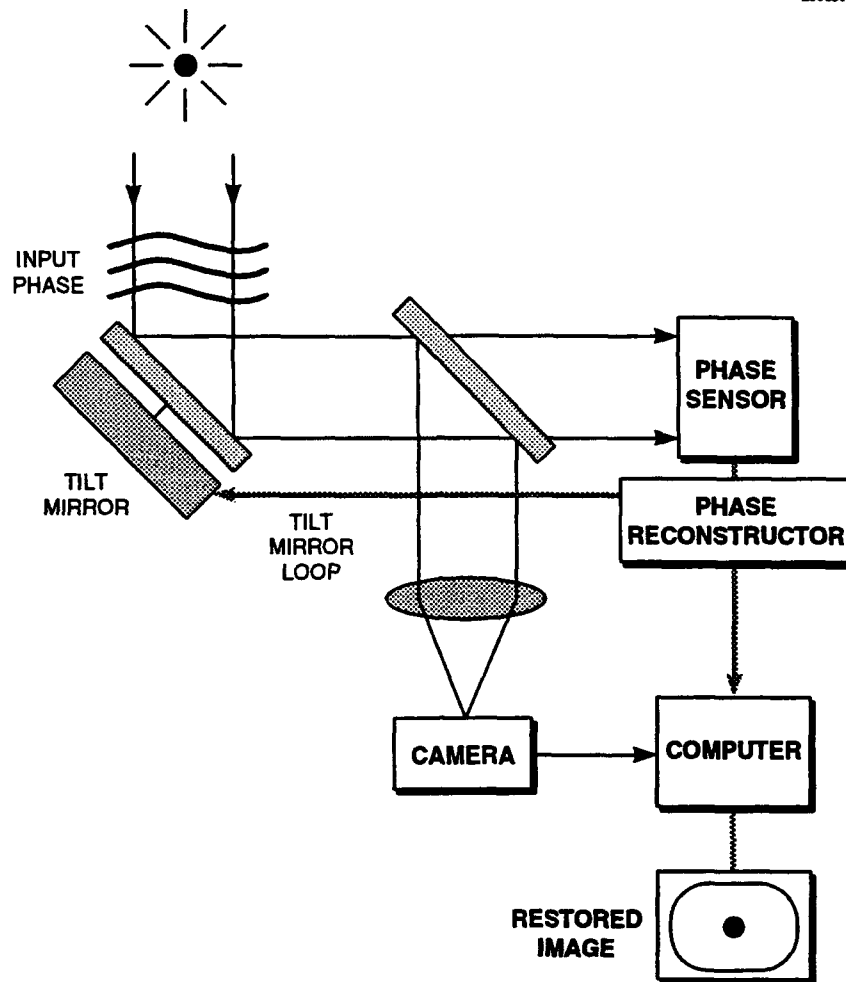
*Figure 4.  Implementation of a data-restoration system that combines speckle imagery and wavefront information. The final image is generated by a computer system that performs the computation indicated by Equation (18).*

## 3.2  COMPARISONS OF EXPERIMENTAL PERFORMANCE UNDER HIGH SIGNAL-TO-NOISE CONDITIONS

Over the last decade a number of adaptive-optics systems have been constructed and successfully operated. Although most of the original work in this field was performed by researchers in the defense community as part of an effort to propagate high energy laser beams from ground to space [9,10], these same techniques have recently been applied to astronomical imaging systems [11]. As a result of these research efforts, there is conclusive evidence that Strehl

13

ratios in excess of 0.2 can be readily achieved when the actuator density and bandwidth of the deformable mirror are chosen so as to match the spatial and temporal characteristics of the atmosphere.

The exploitation of computational techniques to derive nonaberrated pictures of celestial objects from time-resolved speckle imagery and wavefront sensor data is a relatively new concept, and thus far only a few experimental results relating to this approach have been published [27]. This section describes a pair of imaging experiments that were conducted at the Air Force Maui Optical Station test facility in 1990 as part of Lincoln Laboratory's SWAT program. These tests were performed with the aid of a 60-cm telescope and a 241-actuator compensation system and represent the first direct performance comparison between an adaptive-optics system (as described by Figure 3) and a passive image reconstructor (outlined graphically in Figure 4). The same hardware structure was used to provide both sets of data; closed-loop phase correction was achieved by applying the measured pupil-plane phase distortions to the deformable mirror, whereas open-loop phase and image data (collected at the beginning of each closed-loop sequence) were input to the computational reconstructor. The results of two separate compensation experiments are now described.

### 3.2.1 Single-Star Compensation Experiment

On 25 June 1990, Vega was used as both the target star and light source for the wavefront sensor of the SWAT system. This source was sufficiently bright (magnitude 0) to supply approximately 1,400 photons per subaperture over a dwell time of 2 ms. To further improve the sensitivity of the phase sensor, the system was programmed to perform the Hartmann centroid calculation with only the central pair of pixels in each 4-pixel subaperture. The adaptive-optics system was run in the multipulse accumulate mode (5-pulse accumulation) at a 10-Hz repetition rate. The $r_o$ value, based on the figure error of the uncompensated beam, was of the order of 6 cm (compared to an aperture-plane actuator spacing of 3.5 cm). The system's spectral bandwidth was approximately 100 nm centered at 470 nm.

Figure 5 tabulates the short-exposure Strehl for a sequence of 20 phase-compensation experiments from data file SW9006252225. For each measurement the uncompensated beam was recorded with a flat phase imposed on the deformable mirror, whereas the compensated image represents the end result of a sequence in which 5 phase measurements and phase corrections were made within a period of 12.5 ms. On average, the adaptive-optics system improved the Strehl ratio by a factor of 5.

14
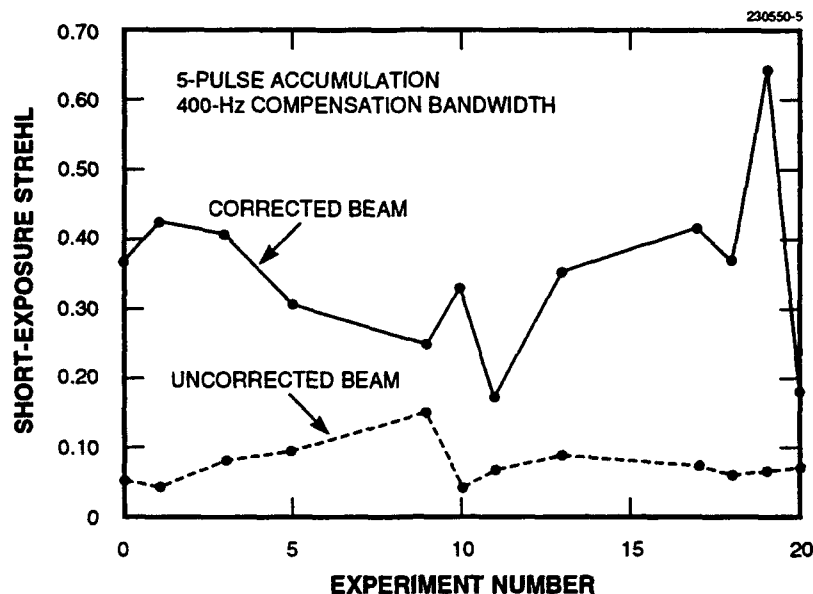
*Figure 5.   Far-field Strehl estimates of the Vega results as a function of experiment number for a series of 20 experiments.  The Strehl average for the uncorrected data is 0.07 and the average corrected Strehl is 0.35.*

Figure 6 compares a set of images obtained from an ensemble average of 20 open- and closed-loop adaptive-optics experiments (tilt loops were closed in both cases) with a computational reconstruction derived from the process outlined in Equation (8.b).  As indicated in this figure, the Strehl of the speckle-reconstruction image is a factor of 2 lower than that achieved with the compensation system, but is about three times better than the uncorrected-image Strehl.  A comparison of the corresponding point spread functions is given in Figure 7; these results are consistent with the previous illustration, and the diameter of the beam formed by the adaptive-optics system is about 50% smaller than the profile of the speckle-reconstruction image.

### 3.2.2   Binary Star Compensation Experiment

Although the data presented in Figures 6 and 7 appear to clearly demonstrate the efficacy of speckle reconstruction, they do not prove that complex details can be faithfully recovered from a non-point-source object.  To supply such proof, imagery from the binary star Castor was recorded on 12 January 1991.  The Castor system contains two stars with an angular separation of 11 $\mu$rad and a combined visual magnitude of 2.9.  For this test the wavefront sensor was operated with a dwell time of 2 ms, whereas the far-field camera was allowed to integrate for 10 ms during each frame.

15

230550-6

COMPENSATED IMAGE
STREHL ≈ 0.26

SPECKLE RECONSTRUCTION
STREHL ≈ 0.12

UNCOMPENSATED IMAGE
STREHL ≈ 0.04

*Figure 6.    Comparison of open- and closed-loop images with the speckle reconstruction of 20 uncompensated frames.  The field of view of these images is 19 μrad.  To obtain the speckle-reconstruction image, the value of e used in Equation (8.b) is $10^{-4}$.*

16
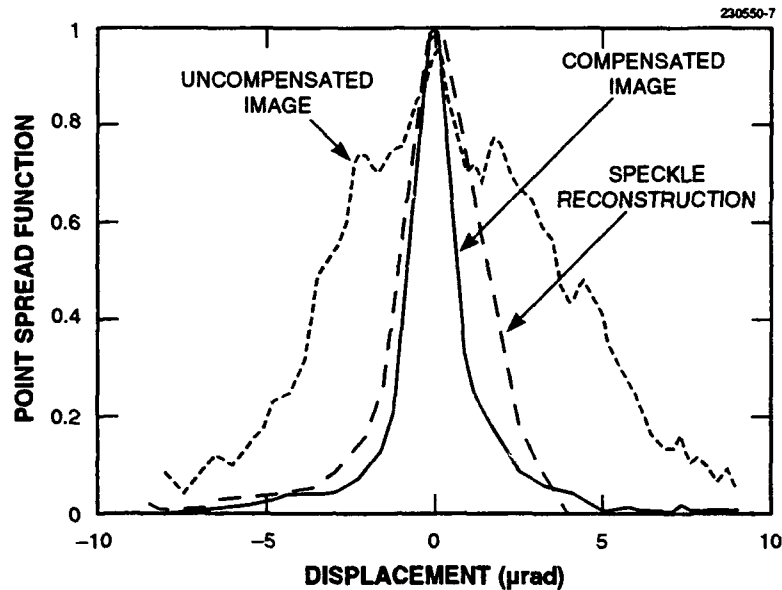
*Figure 7. The point spread function of a speckle reconstruction of Vega is compared with the open- and closed-loop images obtained with the phase-compensation system. The diameter of the reconstructed image is approximately 50% larger than that obtained with the adaptive-optics system.*

Figure 8 compares open- and closed-loop images generated by averaging 40 individual camera frames from data files SW9101122255 and 2256A. Tilt jitter between frames was eliminated through the use of a centroid tracker and a fast steering mirror. During this test, the compensation system demonstrated an ability to improve the tilt-removed Strehl by a factor of approximately 2.4. This relatively low improvement factor (as compared with the fivefold improvement achieved in the previous example) is attributed to phase errors resulting from the use of an extended source for a wavefront reference. A detailed discussion of the origin and magnitude of this type of anisoplanatic error is given elsewhere [28].

The output of the image recovery calculation is illustrated by the central portion of Figure 8. As indicated in Equation (8.b), the most critical aspect of this process involves the array product of the pupil-plane phase data, or $OTF$, and the Fourier transform of the focal-plane image, represented by $\mathcal{F}\{I'\}$. It was discovered that considerable care was required to correctly match the scale and orientation of these two data sets and that any misalignment resulted in a corruption of the original image. Once the input matrices were properly aligned and scaled, a Strehl improvement of approximately 1.8 was observed in the output. This improvement factor is about 25% lower than that achieved by the adaptive-optics system.

Although the comparisons given in Figures 6 and 8 show the images produced by the adaptive-optics system to be superior to those obtained through computational recovery, it should be noted that the spectral bandwidth of the focal-plane data was not ideally suited for this recovery

17

process. As described in Section 2.1, the scale of the speckle image produced by atmospheric turbulence is linearly dependent on wavelength. Unless monochromatic light is used, some image smearing will result. To first order, the reduction in Strehl due to this effect is estimated to be

$$[\text{Strehl}]_{\text{finite bandwidth}} \approx \left( \frac{\Delta\lambda}{\lambda} \frac{D}{r_o} \right)^2 . \tag{19}$$

Because the SWAT system was operated with a fractional bandwidth of 20% and under turbulence conditions corresponding to a $D/r_o$ of approximately 10, the Strehl component due to finite bandwidth is estimated to be 0.25. It is not surprising, therefore, that a significant discrepancy in performance was observed in these imaging experiments.

On the basis of these results and the comments made regarding spectral bandwidth, it is highly probable that computational reconstruction can produce images comparable to those obtainable from an adaptive-optics system under high S/N conditions. Most objects of interest to astronomers, however, are extremely dim ($m_V > 15$), and long integration times (often as long as 1 h) are required to obtain acceptable images. Under these conditions the issues of tracking stability, wavefront characterization, and efficient telescope utilization become crucial; these questions are addressed in Section 3.3.

## 3.3 SYSTEM REQUIREMENTS FOR DIM-OBJECT IMAGING APPLICATIONS

To produce a well-compensated image of a very dim object, three requirements must be satisfied: (1) a fiducial star in close proximity to the target object must be located to drive the tracking system necessary for image stabilization, (2) a reference beacon collinear with the target object must be generated to provide light for the wavefront sensor, and (3) a sufficient number of short-exposure images must be recorded and subsequently integrated to accumulate a signal that is well above the photon noise limit. The design constraints that derive from the first two requirements are identical for the adaptive-optics and computational-reconstruction systems.

### 3.3.1 Design Requirements for Tracking and Wavefront Sensing

Designers of adaptive optics systems find it convenient to divide the effects of turbulence into tilt jitter, which can be compensated with a two-axis tracking mirror, and high-spatial-frequency figure error, which is corrected by the deformable mirror. Each effect has an associated isoplanatic angle, which defines the allowable separation between the reference source and the target object.
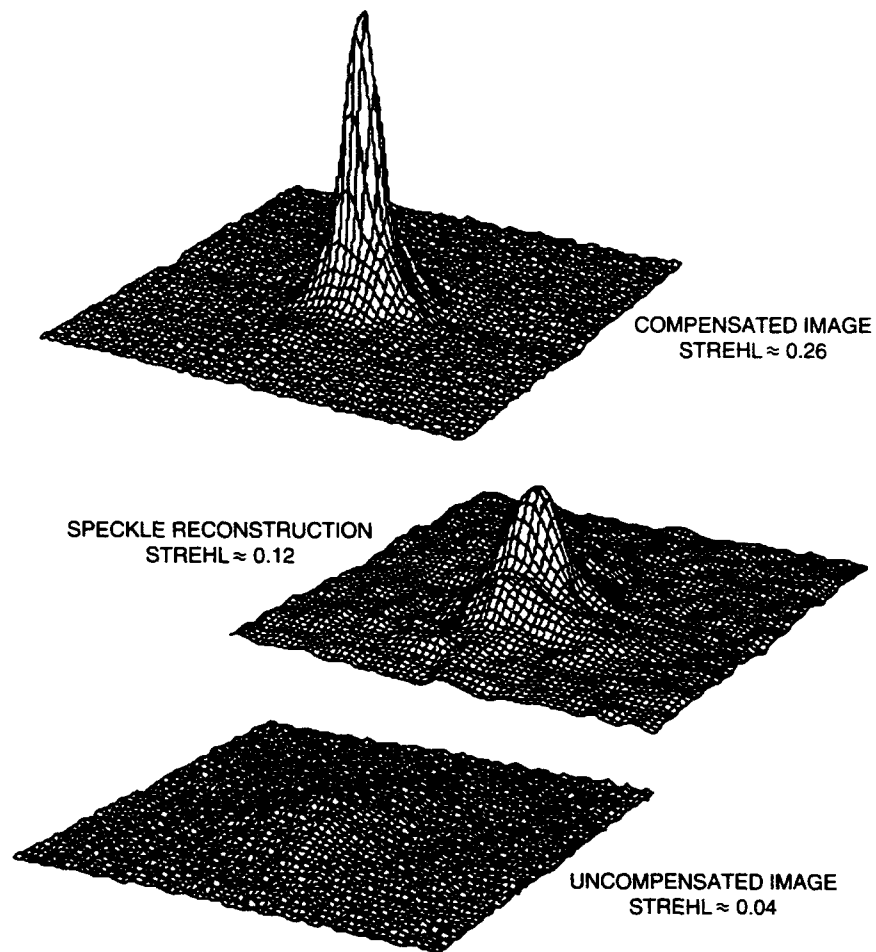
230550-8
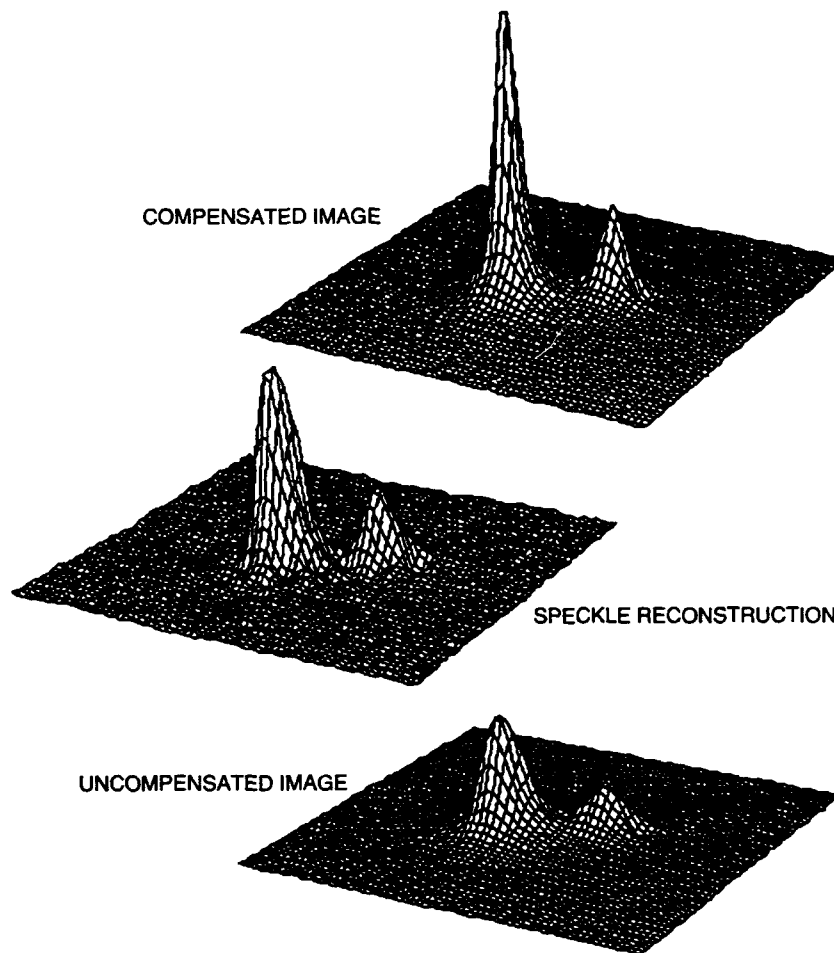


*Figure 8. Comparison of open- and closed-loop images with the speckle reconstruction of 40 uncompensated frames. The field of view of these images is 72 µrad.*

Because tilt involves only the lowest spatial frequencies seen by the telescope, its isoplanatic angle is significantly larger than that for figure; furthermore, the tracking reference can be dimmer than the figure-error reference by as much as six or seven stellar magnitudes. For wavelengths longer than 1 µm, there is a high probability that a suitable tracking star can be located for any celestial object of interest [28].

Natural stars provide a poor reference for wavefront sensing because sufficient light must be provided to each $r_0$-sized section of the aperture to allow local changes in phase to be accurately measured. The combination of the brightness requirement (~ 10th magnitude) and small isoplanatic angle (~ 10 µrad) result in a fractional sky coverage that is well below 1% [28].

An alternative means of generating a reference source for wavefront sensing was first proposed in the early '80s. This concept involves the projection of a pulsed laser beam along the line of sight to the target object and a time-gated measurement of photons that are backscattered by the atmosphere, which, as indicated in Figure 9, is equivalent to the placement of an artificial source near the top of the earth's atmosphere. This measurement technique has recently been experimentally verified [12,18,19], and the results of these tests are found to be in good agreement with theoretical predictions [29]. An optimal system design, which uses resonant backscatter from a stable layer of sodium situated at an altitude of 90 km, requires a pulsed laser capable of transmitting about 10 W of average power to achieve good compensation at 1 μm.
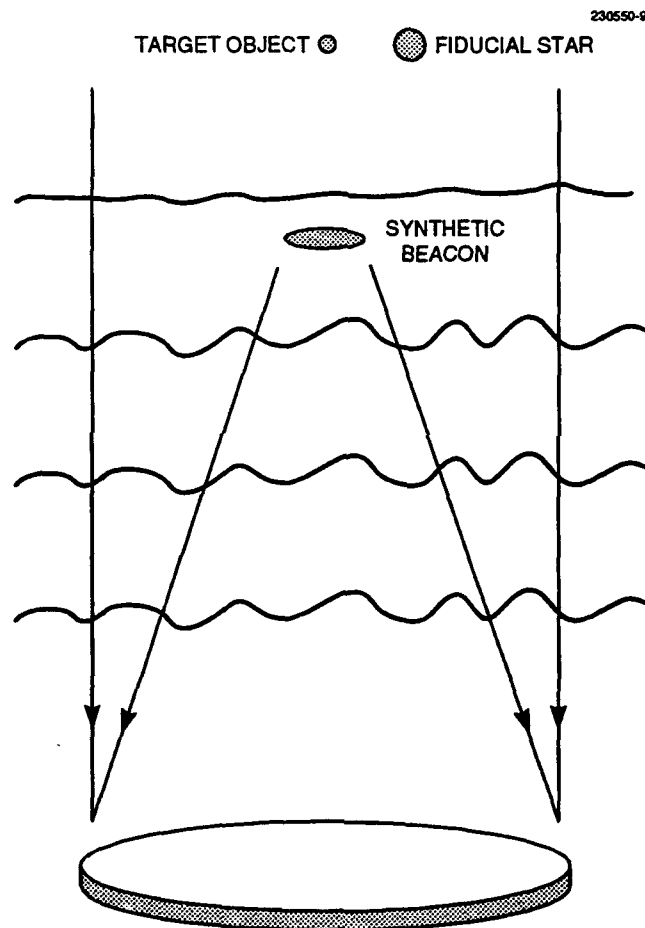


*Figure 9. Geometry essential for dim-object imaging. The fiducial star is used by the tracking system to stabilize a long-exposure image of the target object. The synthetic beacon, produced by a laser beam scattered by the atmosphere, provides the reference source for the wavefront sensor.*

20

### 3.3.2 Comparison of Focal-Plane Data-Integration Requirements

Efficient utilization of astronomical telescopes is an important issue when exposure times of the order of an hour are required to produce high-contrast imagery. In this regard, adaptive optics systems, which achieve a real-time correction of wavefront errors, have significant advantages over computational reconstruction techniques.

It has been shown that the spectral-bandwidth requirement for speckle reconstruction is fairly restrictive, typically resulting in a factor-of-10 reduction in the available broadband radiation. For very dim targets there is a further loss associated with the probability that an individual speckle component will contain all the spatial information necessary for the image recovery process. Whereas an adaptive-optics system essentially collapses all the speckle elements onto a single image that can be integrated indefinitely, the construction of the Fourier plane specklegram (described in Section 2.1) can only occur if each speckle is sufficiently illuminated; photons from different speckles or different data frames do not interact coherently and only contribute to background noise.

For a photon-noise-limited detection process, the signal-to-noise ratio of a long-exposure image corrected by an adaptive-optics system is proportional to the square root of the total number of collected photons

$$[S/N]_{\text{adaptive optics}} \propto \sqrt{M \overline{N}} \,, \tag{20}$$

where $M$ is the number of data frames and $\overline{N}$ is the average number of photons per frame. A description of the S/N properties of a speckle-imaging system is less straightforward, but analyses by Dainty and Greenaway [30] and Beletic [31] have derived the following proportionality for the midrange spatial frequencies:

$$[S/N]_{\text{speckle reconstruction}} \propto \sqrt{\frac{\sqrt{M} \,\overline{N}}{n_{sp}}} \,. \tag{21}$$

The parameter, $n_{sp}$, used in this expression represents the average number of speckles per data frame, which is proportional to $(D/r_o)^2$ for a collector having an aperture diameter, $D$. A comparison of Equations (20) and (21) shows that only a small fraction of the collected photons provide useful information for speckle reconstruction:

$$[\text{Effective Throughput}]_{\text{speckle reconstruction}} \propto \frac{1}{(D/r_o)^2 \sqrt{M}} \,. \tag{22}$$

For exposures of a few minutes duration under nominal seeing conditions, this factor can easily be as small as $10^{-4}$.

21

On the basis of this analysis, it was concluded that a data reconstruction approach is best suited for situations in which the target object is relatively bright or when efficient utilization of the telescope facility is not a concern; in such situations it may be cost-effective to construct a system having no active control elements. A computational reconstructor would be particularly attractive for applications in which natural sources for wavefront sensing have a high probability of occurrence, thereby also eliminating the need for a synthetic-beacon laser.

# 4. RESTORATION OF DATA COLLECTED BY THINNED-APERTURE TELESCOPES

Section 3 discussed the use of speckle interferometry to ameliorate optical distortions due to atmospheric turbulence, but it was also found that the net information content is very low when only a few photons are collected during a single atmospheric time constant. There are, however, other applications of this data-processing concept that do not suffer from the problem of low throughput efficiency. One such application is the restoration of images generated by thinned-aperture optical systems.

For the purpose of this analysis, consider the telescope configuration shown in Figure 10. This three-petal shape represents a lightweight satellite structure that could be stowed compactly prior to deployment in space. This specific design has a fill factor of 10%.



230550-10

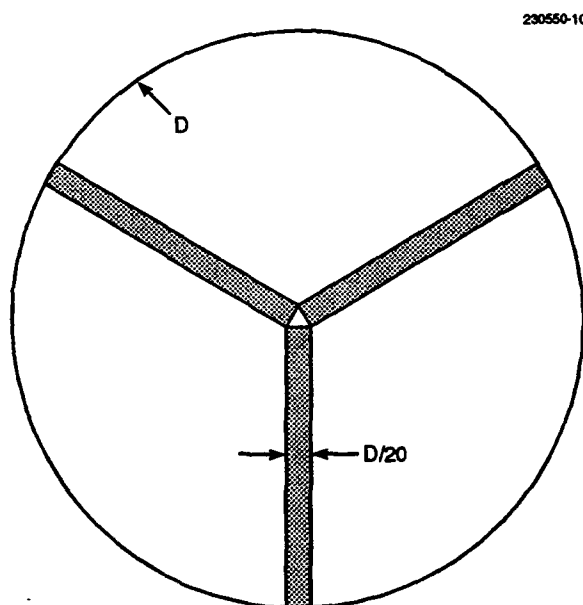*Figure 10. Illustration of a three-segment thinned aperture having an outer diameter of D and segments of width D/20. The collection area of this design is approximately 10% of the full aperture.*

A sparse array offers two significant advantages compared to conventional filled-aperture telescopes.

- As a result of its much lower weight, it is much cheaper to fabricate and deploy.

23

- It can be scaled to very large apertures (i.e., many tens of meters), thus allowing the construction of very high-altitude, high-resolution systems.

To demonstrate the viability of this design, however, it must first be shown that the quality of the imagery produced by such a telescope is comparable to that obtainable from a full-aperture system.

Three distinct tasks are performed in this section. First, a data-processing algorithm is developed that produces an optimal restoration of two-dimensional images that have been corrupted by aperture thinning and additive noise. Second, this algorithm is applied to the output of a telescope having a 10% fill factor; a signal-to-noise ratio between 10 and 30 is shown to be adequate to achieve near-diffraction-limited performance from the restored data. Third, the dwell-time requirements for an 8-m geosynchronous reconnaissance satellite are computed.

## 4.1 DATA RECOVERY ALGORITHMS FOR THINNED APERTURES

The modulation transfer functions for a circular aperture and the thinned-aperture configuration shown in Figure 10 are compared in Figures 11 and 12, respectively. The thinned-aperture *MTF* is nonzero over most of the region covered by the filled-aperture transfer function, but the midrange frequency components have been greatly attenuated. Under ideal (noiseless) conditions, most of this information contained in the original scene can be recovered through a process that is described next.

### 4.1.1 Reconstruction of Noiseless Data

The recovery process for noise-free conditions is relatively straightforward and derives from standard techniques developed for speckle interferometry. As shown in Figure 13, the structure of this point spread function is dominated by a single diffraction-limited peak that contains about 10% of the total power; most of the remaining power is distributed among an array of six arms that emanate from the central core. Although this function extends over a wide angular region, due to the well-developed central peak with its near-radial symmetry, chromatic-smearing effects will not result in significant distortions in the image-reconstruction process. Therefore, unlike the restrictions necessary for turbulence-induced speckle imaging, sensors having a wide spectral bandwidth can be used with thinned-aperture telescopes.

For a two-dimensional image, $I_{ta}$, generated by the thinned array, the best estimate of the image obtainable from a circular aperture is derived from the simple Fourier space transformation

$$\tilde{I}_c = \mathcal{F}^{-1}\left\{\left[\frac{(MTF)_{\text{full aperture}}}{(MTF)_{\text{thinned aperture}}}\right]\mathcal{F}\{I_{ta}\}\right\} . \tag{23}$$

The multiplicative factor formed by the ratio of the full- and thinned-aperture *MTF*s is largest at the midrange frequencies. This operation produces the effective system *MTF* illustrated in Figure 14.

24
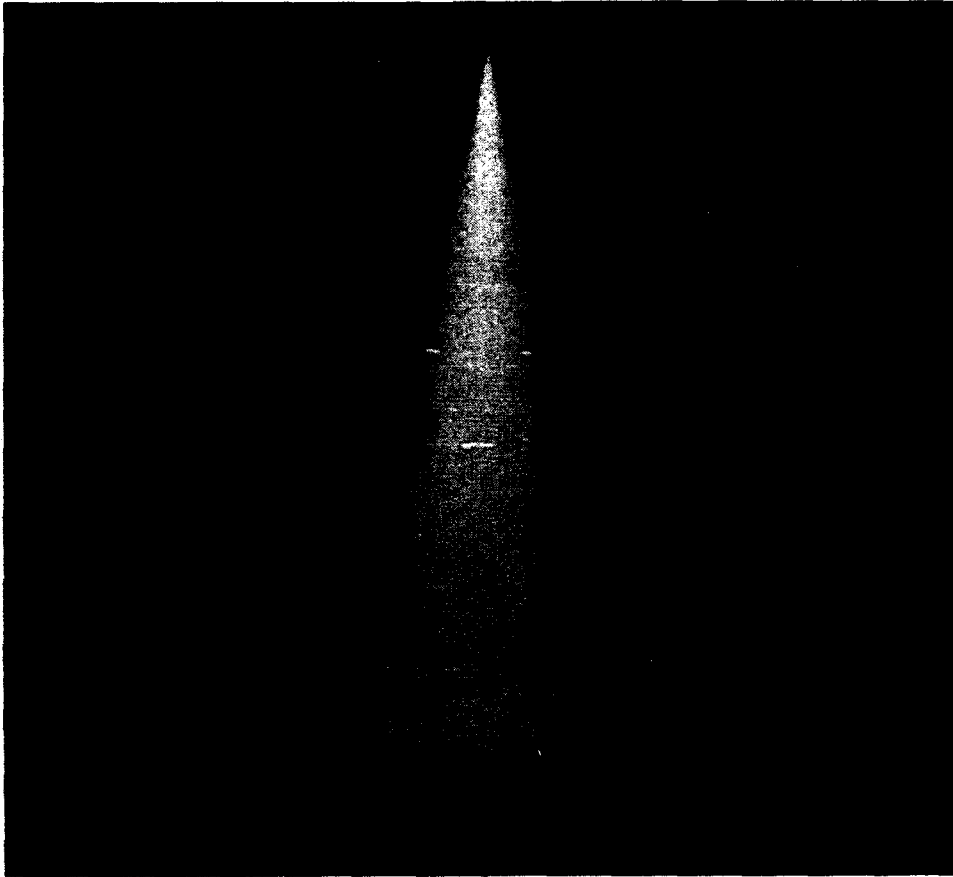
*Figure 11. Modulation transfer function of a circular aperture.*
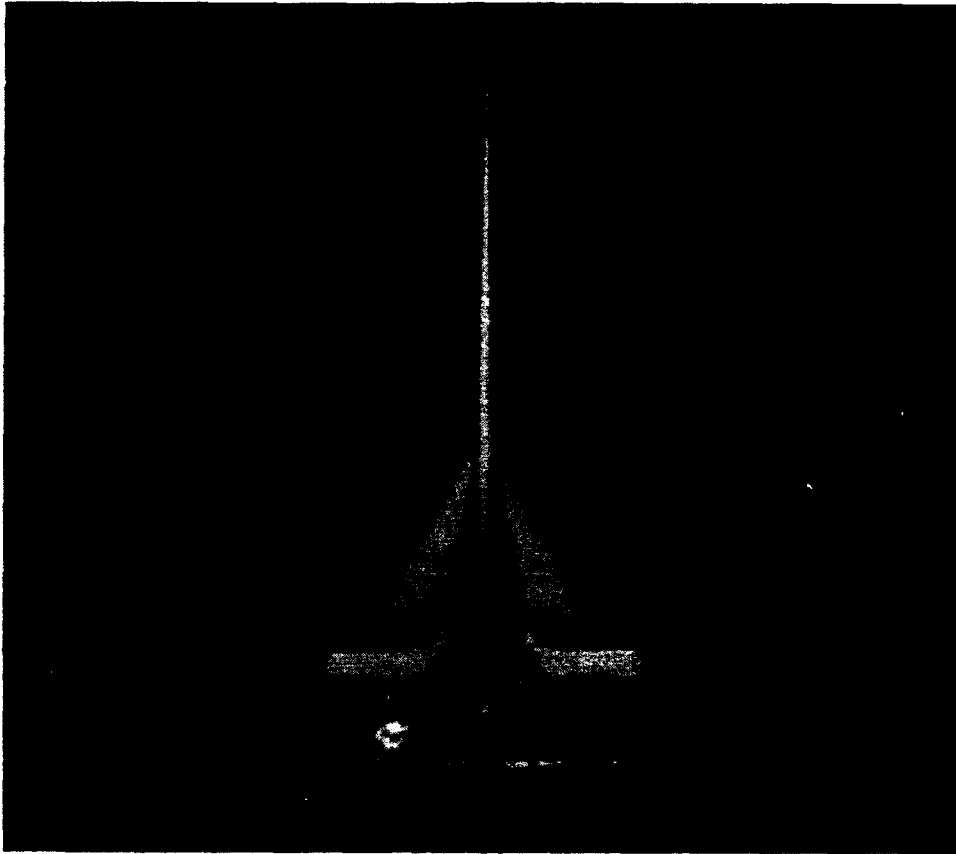
*Figure 12. Modulation transfer function of the thinned-aperture telescope depicted in Figure 10.*

26

230550-11
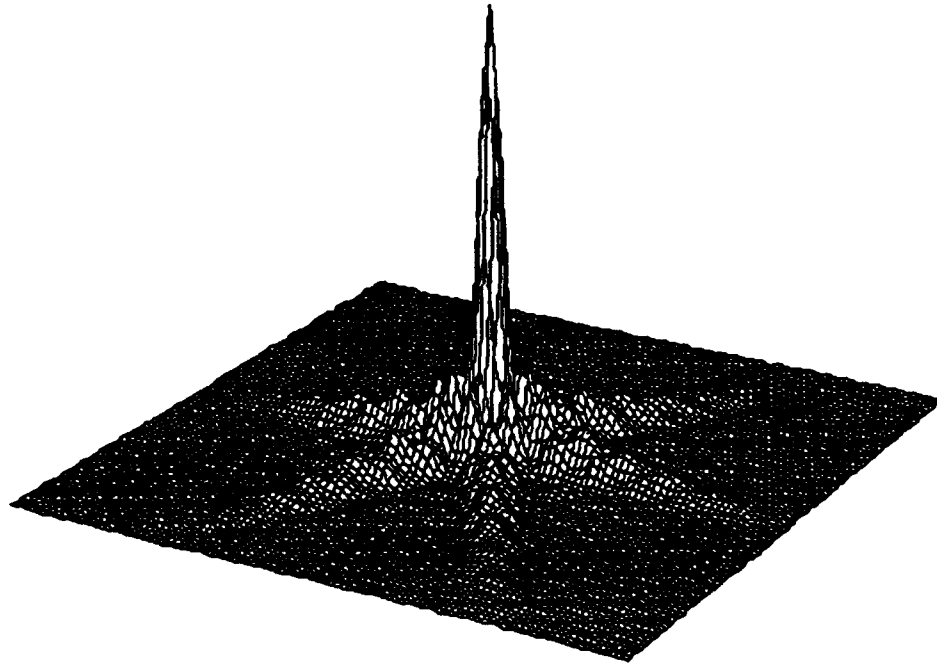
Figure 13. *Point spread function of the three-petal telescope. Approximately 10% of the total power is contained in the central diffraction-limited peak.*
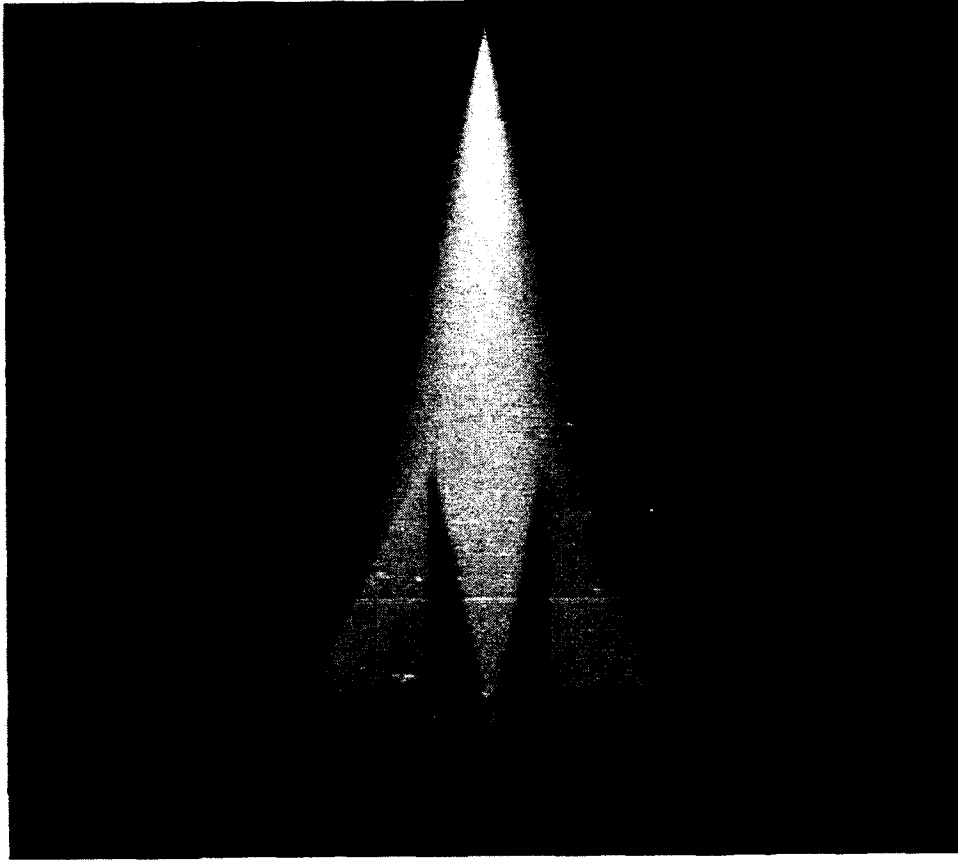
*Figure 14. Effective MTF of a thinned-aperture system incorporating the data processing technique defined in Equation (23).*

## 4.1.2 Optimal Reconstruction of Finite-Noise Data

The computational procedure outlined in Equation (23) typically results in an extremely noisy reconstruction due to the high gain that is applied at spatial frequencies for which the S/N level is less than unity. This effect can be avoided by using the expression developed for finite-noise scenarios derived in Section 2.3. From Equation (18) the following expression is obtained:

$$\tilde{I}_c = \mathcal{F}^{-1}\left\{\left[\frac{(MTF)_{\text{thinned aperture}} (MTF)_{\text{full aperture}}}{(MTF)^2_{\text{thinned aperture}} + F_n/F_o}\right] \mathcal{F}\{I_{ta} + n\}\right\} \quad , \qquad (24)$$

28

where $F_o = |\mathcal{F}\{I\}|^2$ and $F_n = |\mathcal{F}\{n\}|^2$ are the power spectral density functions associated with the object and the system noise, respectively. To complete this discussion the functional form of $F_o/F_n$, which is proportional to the square of the signal-to-noise ratio of the optical power (or electrical voltage), must be specified.

For scenes containing normal terrain it has been found that the autocorrelation can be accurately modeled as a first-order Markov process [32],

$$\mathfrak{R}_o(\vartheta) = \sigma_o^2 \, e^{-\left|\vartheta/\vartheta_\rho\right|} \quad , \tag{25}$$

where $\vartheta$ represents an angular separation within a two-dimensional object space, $\vartheta_\rho$ is the correlation angle, and $\sigma_o^2$ is the intensity variance of the scene. The power spectral density function is the Hankel transform of this expression:

$$F_o(f) = \frac{2\pi \, \sigma_o^2 / \vartheta_\rho}{\left[(2\pi f)^2 + 1/\vartheta_\rho^2\right]^{3/2}} \quad . \tag{26}$$

The noise is assumed to be white, but it is important to establish the correct normalization factor. For a discrete data-collection system the signal will be constant over the dimensions of a pixel, which correspond to the angular displacement $\vartheta_{\mathrm{pix}}$. When the noise is uncorrelated this model results in a triangular-shaped autocorrelation function having a value of $\sigma_n^2$ at the origin; the associated power spectral density function in rectangular coordinates is

$$F_n(f_x, f_y) = \sigma_n^2 \, \vartheta_{\mathrm{pix}}^2 \left\{ \frac{\sin^2\left(\pi \vartheta_{\mathrm{pix}} f_x\right)}{\left(\pi \vartheta_{\mathrm{pix}} f_x\right)^2} \right\} \left\{ \frac{\sin^2\left(\pi \vartheta_{\mathrm{pix}} f_y\right)}{\left(\pi \vartheta_{\mathrm{pix}} f_y\right)^2} \right\} \quad . \tag{27}$$

For discrete Fourier transform operations performed over the range $-1/2\vartheta_{\mathrm{pix}} \le f \le 1/2\vartheta_{\mathrm{pix}}$, it is convenient to replace Equation (27) with the approximation

$$F_n(f_x, f_y) \approx \begin{cases} \sigma_n^2 \, \vartheta_{\mathrm{pix}}^2 & |f_x| \le 1/2\vartheta_{\mathrm{pix}} \ \text{and} \ |f_y| \le 1/2\vartheta_{\mathrm{pix}} \\ 0 & |f_x| > 1/2\vartheta_{\mathrm{pix}} \ \text{or} \ |f_y| > 1/2\vartheta_{\mathrm{pix}} \end{cases} , \tag{28}$$

which encompasses the same integrated power. Thus, within the region over which the discrete Fourier transform is performed,

29

$$F_o(f)/F_n(f) \approx 2\pi \left(\frac{\sigma_o^2}{\sigma_n^2}\right)\left(\frac{\vartheta_\rho^2}{\vartheta_{\text{pix}}^2}\right)\left[1+\left(2\pi\vartheta_\rho f\right)^2\right]^{-3/2} \quad . \tag{29}$$

The system *MTF* that results for a signal-to-noise ratio $(\sigma_o/\sigma_n)$ of 10 and a correlation length of 15 pixels is shown in Figure 15; comparisons with the circular aperture and unprocessed *MTF*s are made in Figure 16.

### 4.1.3 Data Restoration with a Convolution Operator

For real-time data-processing applications, it may be computationally advantageous to perform the data restoration with a spatial-convolution operator of limited extent. The form of this operator is obtained from a simple modification of Equation (24):

$$\tilde{I}_c = \left[\underbrace{T_{\text{kernel}} \ \mathcal{F}^{-1}\left\{\frac{(MTF)_{\text{thinned aperture}} \ (MTF)_{\text{full aperture}}}{(MTF)^2_{\text{thinned aperture}} + F_n/F_o}\right\}}_{\text{convolution kernel}}\right] \otimes \left(I_{ta}+n\right) \quad . \tag{30}$$

$T_{\text{kernel}}$ is a two-dimensional truncation function that is used to limit the physical size of the operator; its value is set to unity within the kernel and zero elsewhere.

If this process is to work efficiently, the convolution kernel must be kept as small as possible; on the other hand, good performance can be achieved only if its size is commensurate with that of the thinned-aperture point spread function. Since the central core of the *MTF* is approximately equal to the width of one aperture section, it is expected that $T_{\text{kernel}}$ should be about a factor of 20 larger than the diffraction-limited point spread function of the aperture shown in Figure 10. This point is illustrated in Figure 17, which shows a trace along the horizontal axis over a span of 20 diffraction-limited beam diameters. The absolute value of the filter function outside this region is less than 10% of its value at the origin.

The overall performance of a 64x64-pixel kernel (roughly equivalent to 20 diffraction-limited beam diameters) is illustrated in Figure 18. A comparison with the Fourier deconvolution *MTF* (indicated by the solid line) shows that the truncation of the convolution kernel results in a minor perturbation of the system response function at very low spatial frequencies. Although this effect introduces some distortion in the final image, it is unlikely that a significant loss of data results. Through the judicious selection of kernel size and the implementation of appropriate apodisation procedures, one can achieve a balance between image quality and computational speed that is best matched to the specific surveillance application.
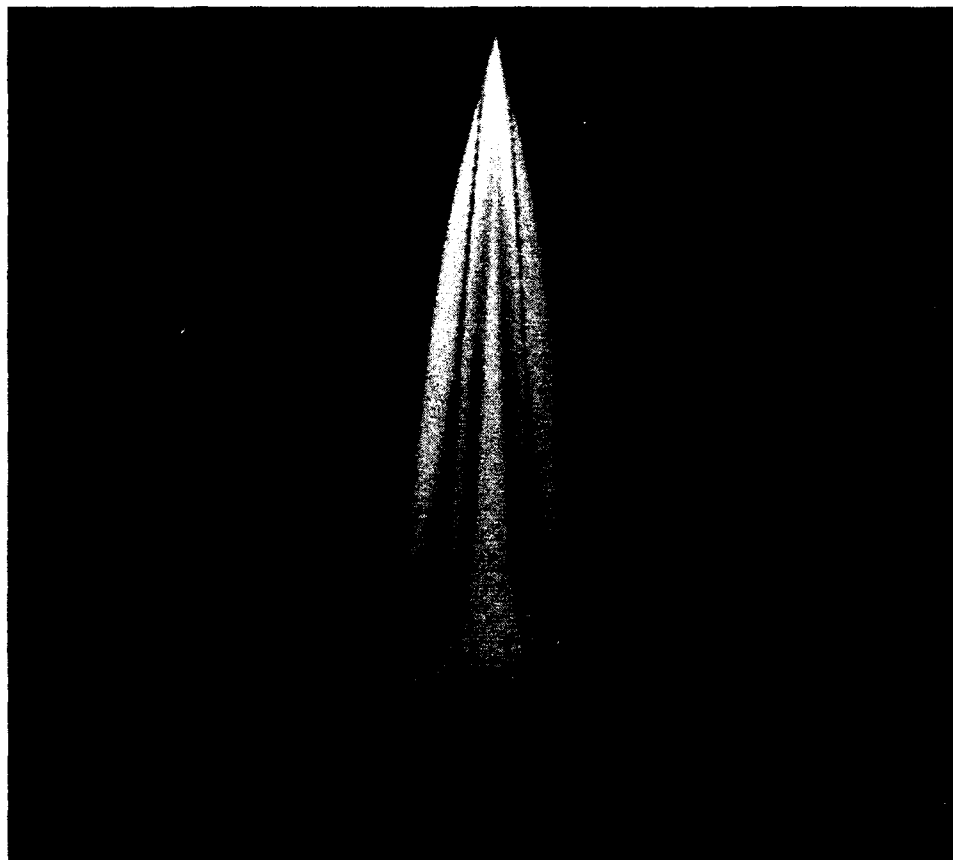
*Figure 15. Effective MTF of a thinned-aperture system incorporating the data processing technique defined in Equation (24). In constructing this plot, a signal-to-noise ratio of 10 and a correlation length of 15 pixels are assumed.*
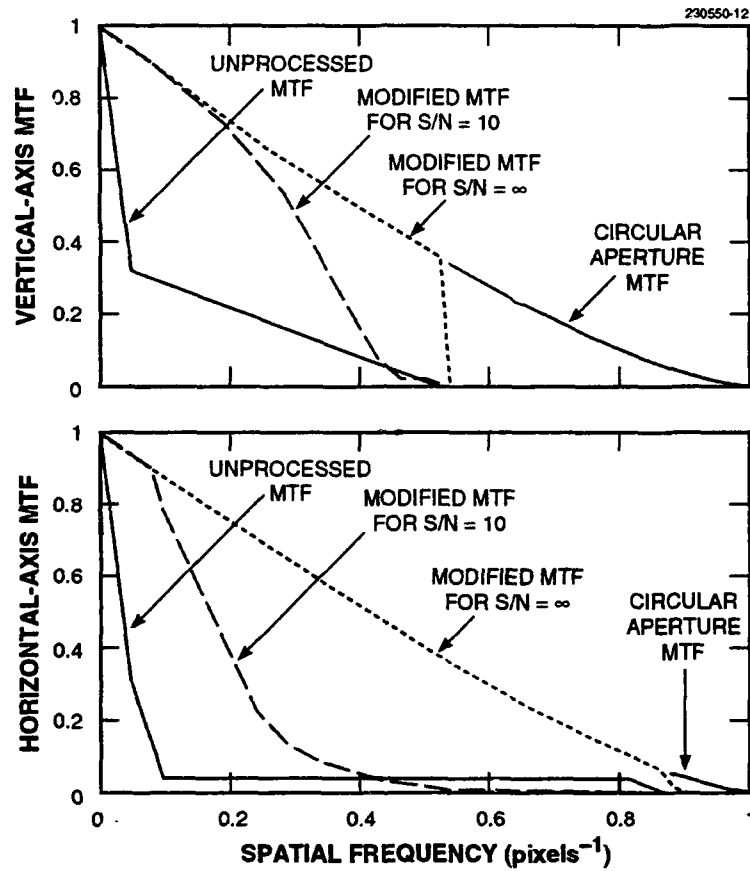
*Figure 16.  Comparison of MTF functions along the (a) vertical and (b) horizontal axes.  For the zero-noise case, the modified MTF of the thinned aperture replicates the circular-aperture MTF for all nonzero values of the function. The effective MTF for S/N = 10 is approximately equivalent to that of a circular aperture of diameter D/2.*

32
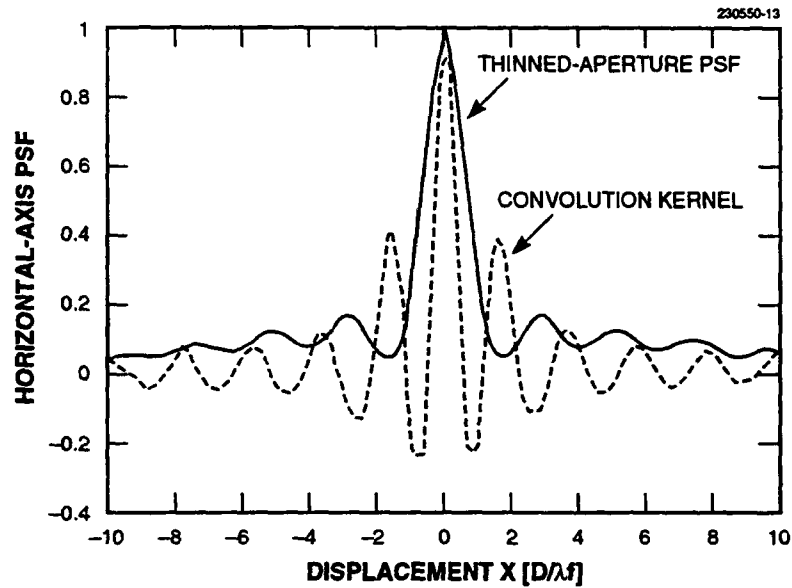
*Figure 17. Representation of the kernel used to perform a convolution reconstruction of the thinned-aperture data.*
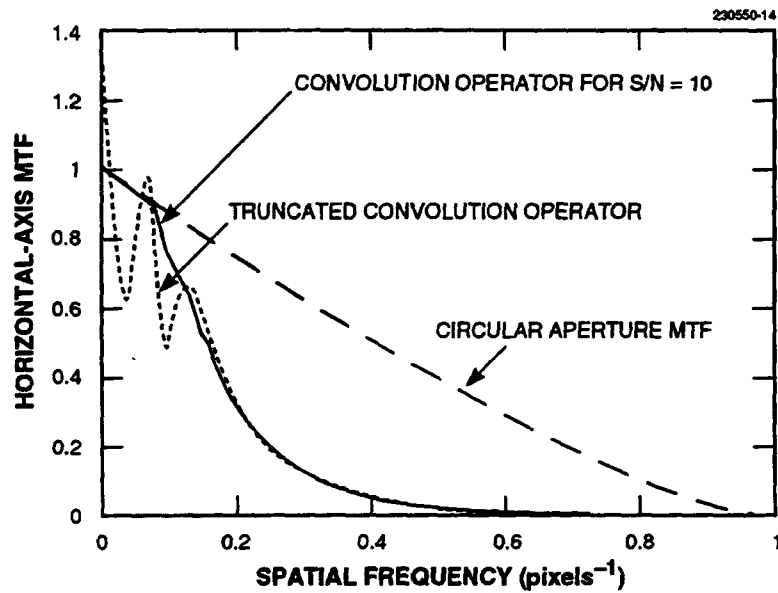


*Figure 18. Comparison of transfer functions obtained with the full convolution kernel and a 64x64-pixel truncated kernel.*

33

## 4.2 EXAMPLES OF IMAGE RECONSTRUCTION FOR A REPRESENTATIVE RECONNAISSANCE SCENARIO

To complete this discussion, the data processing techniques developed in the preceding sections are applied to a pair of digitized data frames. The first of these images is a bar pattern chart that was created to provide a quantitative means to study resolution effects. The second is a terrestrial scene collected by a down-looking infrared (IR) sensor. The diffraction-limited resolution of the IR sensor was equivalent to 3 pixels, that is,

$$d_{pix} = \frac{1}{3} \frac{\lambda R}{D} \, ,$$

where $d_{pix}$ is the ground patch associated with one pixel, $D$ is the aperture diameter, and $R$ is the distance between the sensor and the object. (This value is 50% smaller than the Nyquist requirement.) To simplify the comparative analysis of sensor performance, this same viewing geometry is assumed for the bar patterns.

### 4.2.1 Analysis of Imagery Derived from Bar Patterns

The first of the data files used in this performance analysis consists of a set of 16 horizontal and vertical bar patterns representing feature spacings that are varied from 1 to 8 pixels (shown in Figure 19). Figure 20 gives the image as seen by a noiseless sensor that has been mated to a telescope having a circular aperture of diameter $D$. The viewing geometry, as explained previously, is assumed to provide a diffraction-limited resolution equivalent to 3 pixels. The result obtained by convolving the point spread function of the full aperture with the original bar pattern is found to be completely consistent with diffraction theory; the bars that are separated by a single pixel cannot be resolved in either the horizontal or vertical directions.

The noise-free output from the tri-petal collector is given in Figure 21, where a dramatic reduction in contrast is seen over the entire image, as well as the loss of the horizontal pattern with the 2-pixel spacing. In the reconstruction of this image, shown in Figure 22, all the nonzero frequency components have been completely restored. The degree of restoration is further illustrated in Figure 23, in which a horizontal line traces through the third set of bar patterns (corresponding to bar spacings of 5 through 8 pixels) are compared.

Figures 24 through 27 show an equivalent comparison for the case in which Gaussian noise corresponding to 5% of the full range of the original image has been added to the sensor output. This measurement scenario is roughly comparable to a signal-to-noise ratio of 10 for the original image; however, as a result of the strong attenuation of the midrange spatial frequencies by the thinned-aperture *MTF*, the ratio of the power spectral density functions of the transmitted signal and the applied noise is close to unity for these scene elements.

A comparison of Figures 25 and 26 shows that the data restoration algorithm defined by Equation (24) has produced a substantial improvement in the overall quality of the thinned-aperture

34

image. Although some of the noise components of the scene are also magnified by this process, the inclusion of the $F_n/F_o$ term in the denominator of Equation (24) guarantees that the final scene is signal dominated. A quantitative comparison is given in the horizontal line traces through the third set of bar patterns in Figure 27. The contrast improvement indicated by the second and third traces shown in this figure represents a clear demonstration of the efficacy of this data-recovery algorithm.
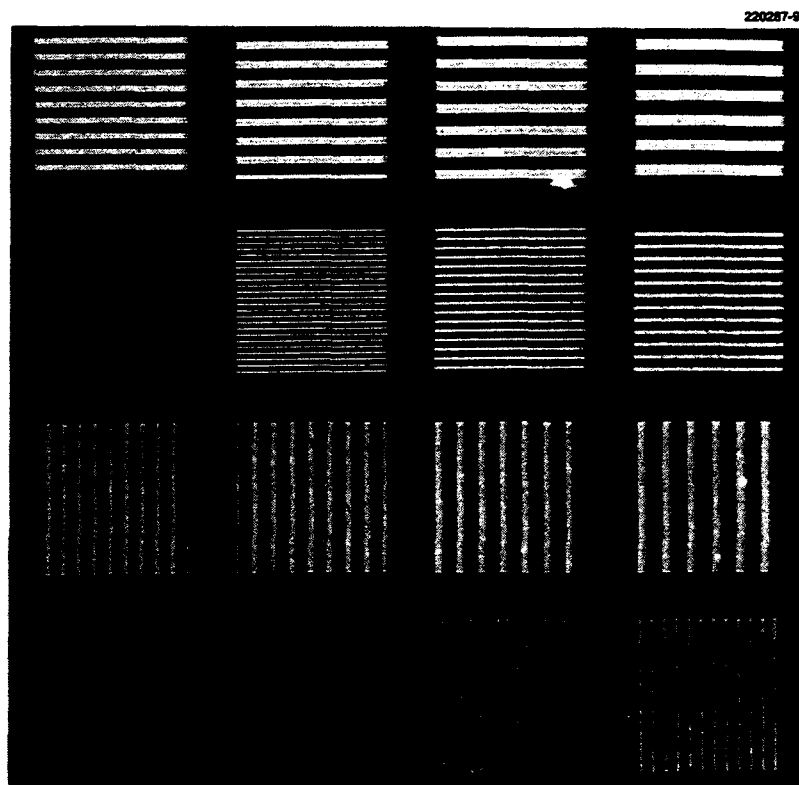


*Figure 19.   Vertical and horizontal bar patterns used to measure the composite resolution of the simulated imaging device.  The bar spacing ranges from one to eight pixels.*
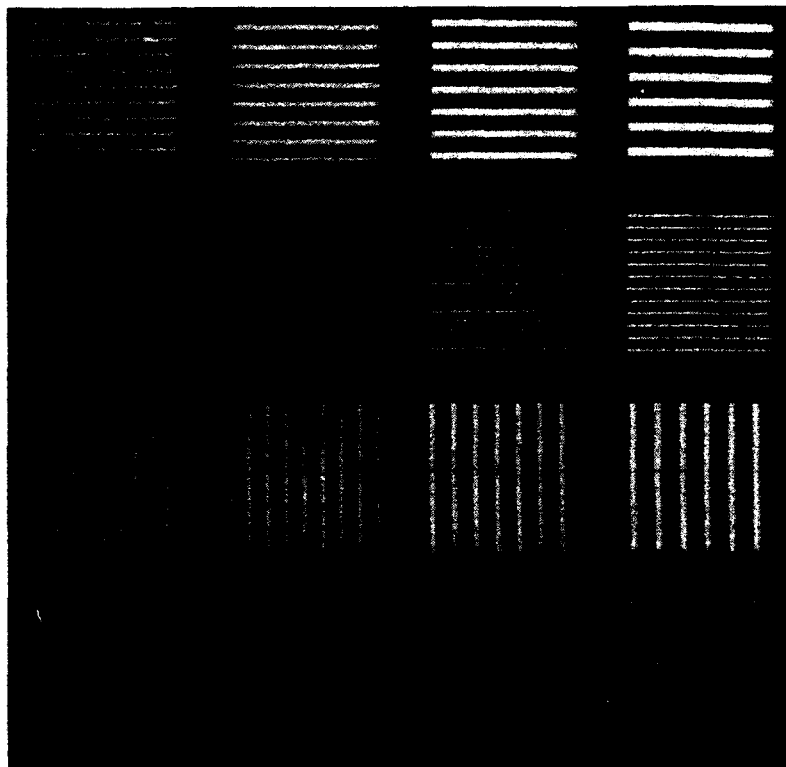
*Figure 20.   Bar pattern chart as seen by the full-aperture system. The system is just able to resolve the pattern in which the bar spacing is two pixels.*

36
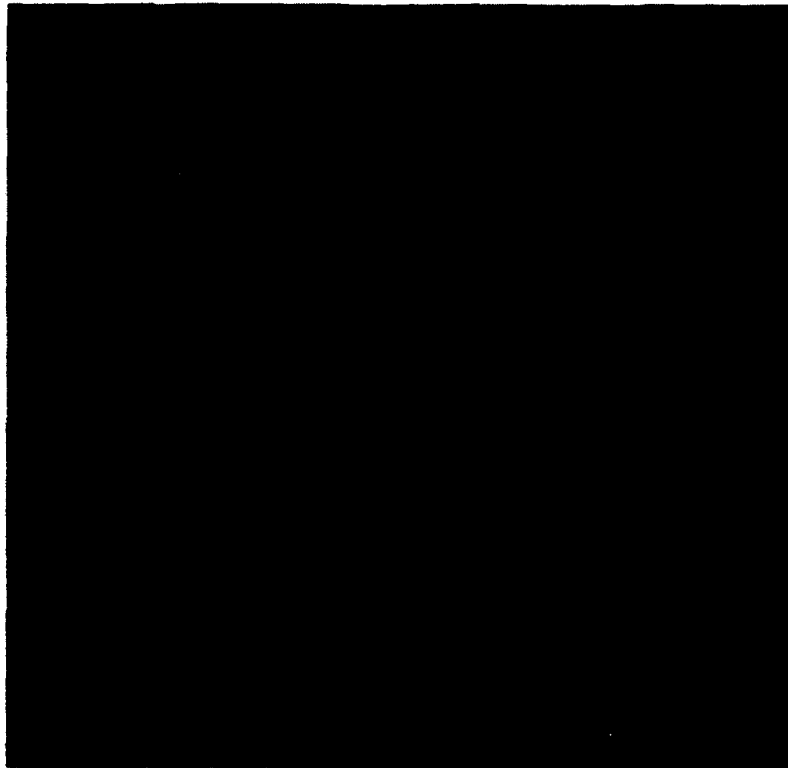
*Figure 21.  Bar pattern chart as seen by the thinned-aperture system.  In the vertical direction the system is just able to resolve the pattern in which the bar spacing is three pixels; its lower limit in the horizontal direction is two pixels.  A substantial reduction in contrast is seen over the entire image.*
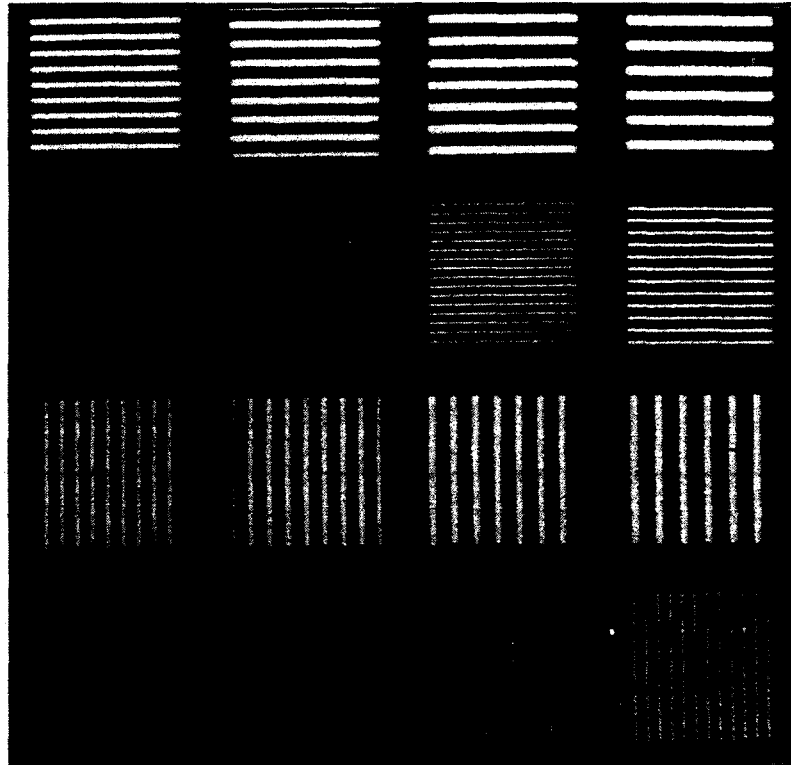
*Figure 22.  Bar patterns produced as a result of processing the thinned-aperture image.  Full contrast has been restored to all spatial frequencies within the resolution limits of the system.*
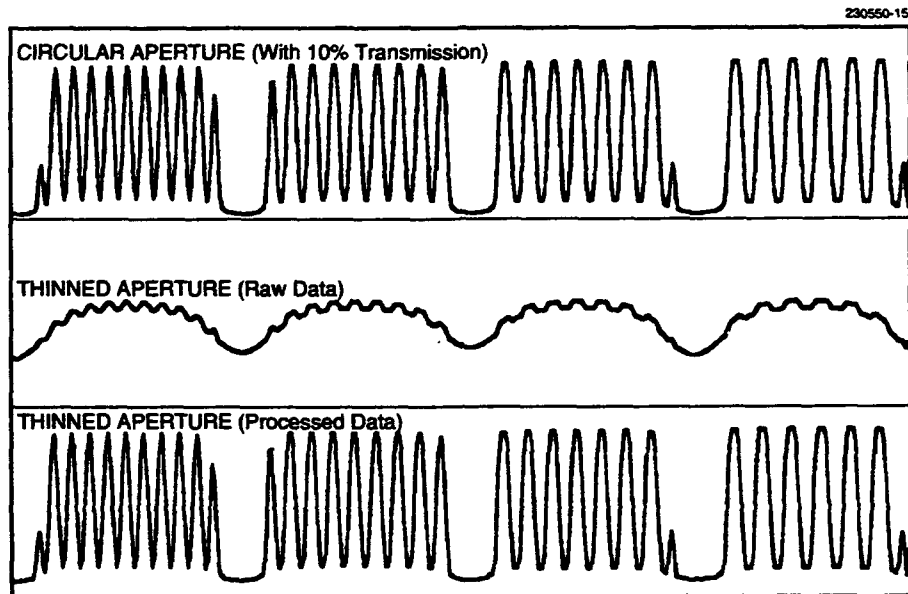
*Figure 23. Horizontal line trace through the center of the third set of bar patterns. (Third row from the top in Figures 20, 21, and 22.) In each trace the bar spacing in the four boxes varies from five to eight pixels. The contrast ratio of the raw data generated by the thinned aperture is approximately 5% of that from the full aperture, but essentially all the original contrast is restored as a result of the data processing.*
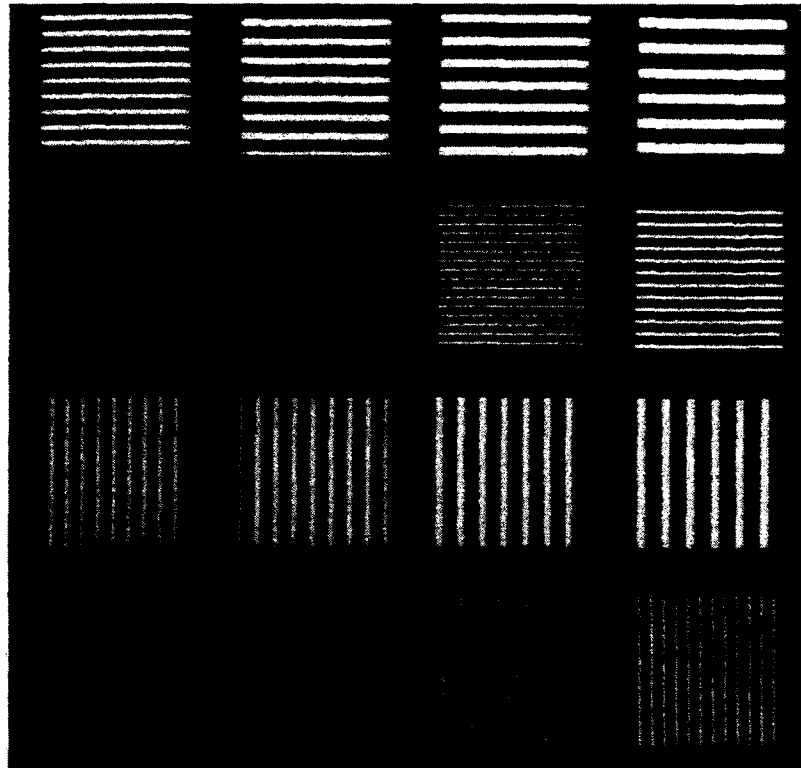
*Figure 24. Bar pattern image from the full-aperture system to which random noise having a standard deviation of 12 counts (5% of the full range) has been added.*
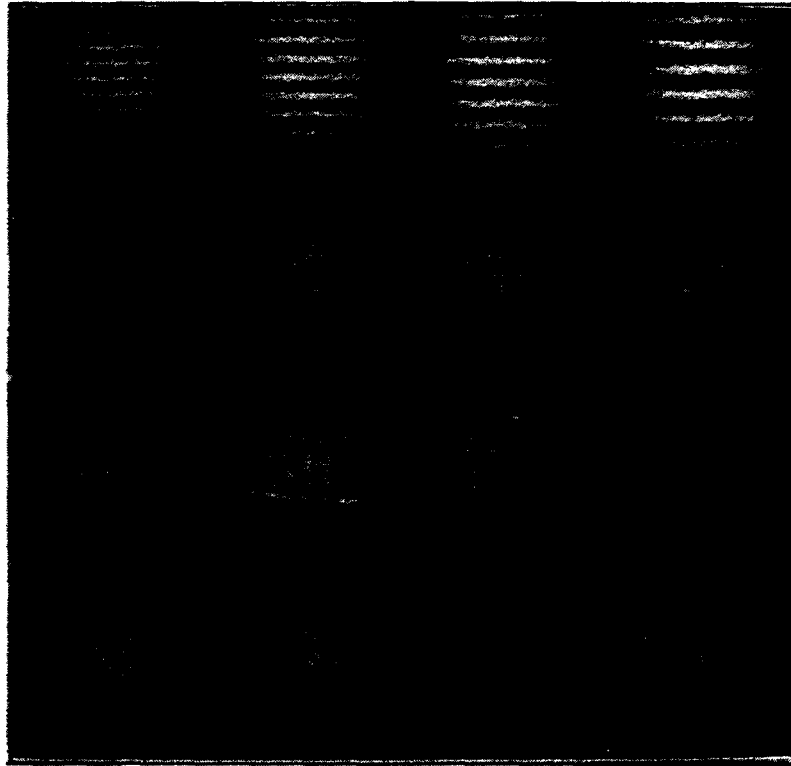
*Figure 25. Bar pattern image from the thinned-aperture system to which random noise having a standard deviation of 12 counts (5% of the full range) has been added.*

41
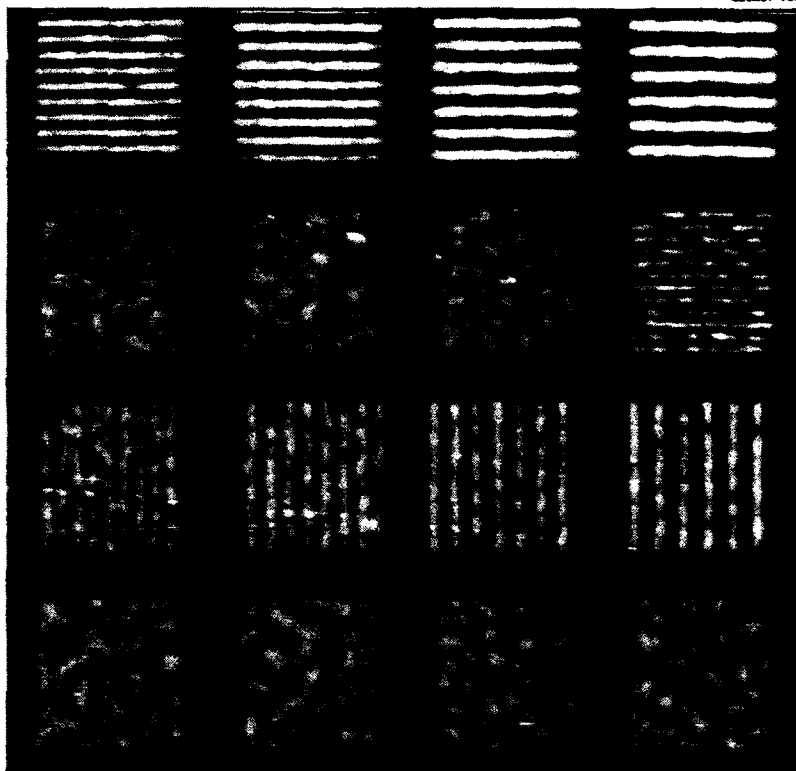
*Figure 26.  Processed image of the bar patterns as viewed by the thinned-aperture system.  Random noise having a standard deviation of 12 counts (5% of the full range) was added to the image prior to the data processing step.*

42
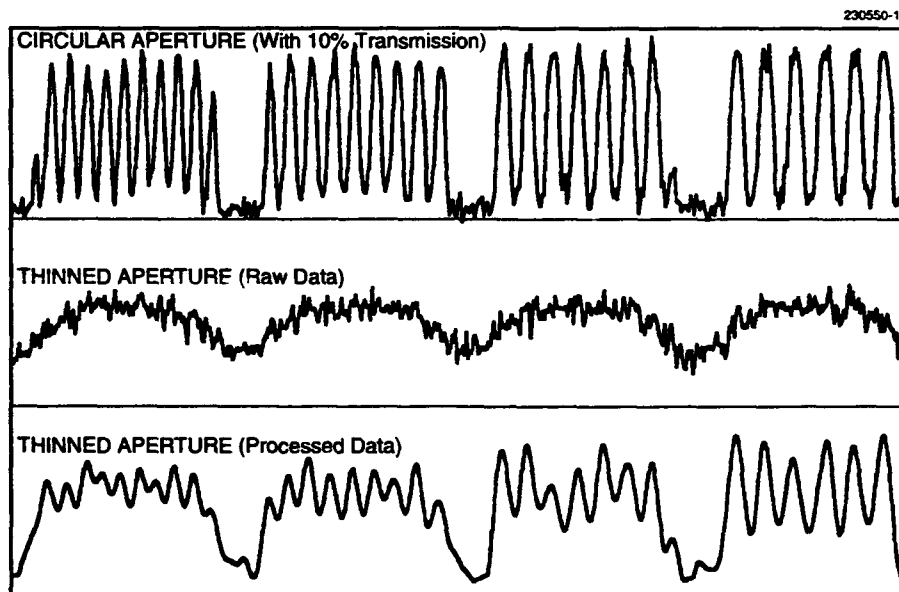
*Figure 27. Horizontal line trace through the center of the third set of bar patterns. (Third row from the top in Figures 24, 25, and 26.) In each trace the bar spacing in the four boxes varies from five to eight pixels. Noise corresponding to 5% of the full range of the original image has been added to the outputs of the circular-aperture system and the raw data from the thinned-aperture system.*

## 4.2.2 Application of the Thinned-Aperture Data Collection and Processing System to a Representative Terrestrial Image

As a further demonstration of the practical utility of a thinned-aperture system when used in conjunction with an appropriate data processor, a Landsat image of Logan Airport in Boston, Massachusetts, was employed in a series of imaging simulations. The original 256x256-pixel picture has a sample spacing of 29 m and covers a 7.4-km$^2$ field of regard. The satellite's band-3 data from its Thematic Mapper, which provides imagery within the 630- to 690-nm spectral region, was selected for this analysis. These data were collected with a 41-cm aperture from an altitude of 700 km; therefore, the point spread function of the instrument had a negligible effect on the image resolution. The correlation length of this data set was computed to be approximately 75 m.

To accurately assess the capability of the processing technique, these Landsat data were first convolved with a circular-aperture point spread function comparable to the dimensions of a single pixel. Specifically, the relationship between the satellite's aperture diameter, altitude, and viewing wavelength was established by the following expression:

$$\frac{\lambda R}{D} = d_{\text{pix}} \quad . \tag{31}$$

The resulting picture, shown in Figure 28, provides a baseline against which the reconstructed images can be compared.

The raw data that would be generated by an aperture having the three-petal geometry illustrated in Figure 10 is shown in Figure 29. The sixfold symmetry of this system point spread function is clearly in evidence, and the smearing is severe enough to destroy all but the grossest details of the image. The degree of recovery achievable using the optimized Fourier-deconvolution process defined in Equation (24) is indicated in Figures 30 and 31. In the first of these illustrations, a signal-to-noise ratio $(\sigma_o/c_n)$ of 10 was assumed. The improvement is significant and image details of the order of a few pixels are discernible, but the overall quality is clearly inferior to that obtainable with a circular aperture. The final picture (Figure 31) represents the output of the deconvolution process for a thinned-aperture image having a signal-to-noise ratio of 100. Comparing Figures 28 and 31 shows that the two are virtually indistinguishable. In general, a signal-to-noise ratio of 30 permits an acceptable level of recovery.

233519-2L
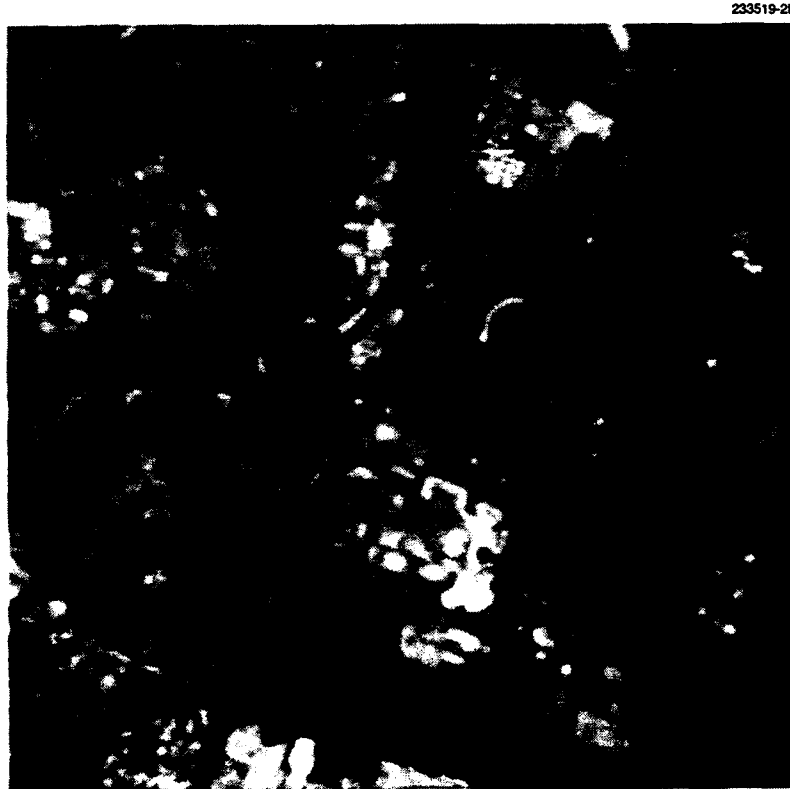


*Figure 28. Visible image of Logan Airport in Boston. The image dimensions are 256x256 pixels and each pixel represents a ground displacement of 29 m. Original data were convolved with the point spread function for a circular aperture so that the resulting image quality is diffraction limited.*

44

*Figure 29. Image of Logan Airport as seen by the thinned-aperture optical system. Smearing effects are due to the extended arms of the aperture point spread function.*

45
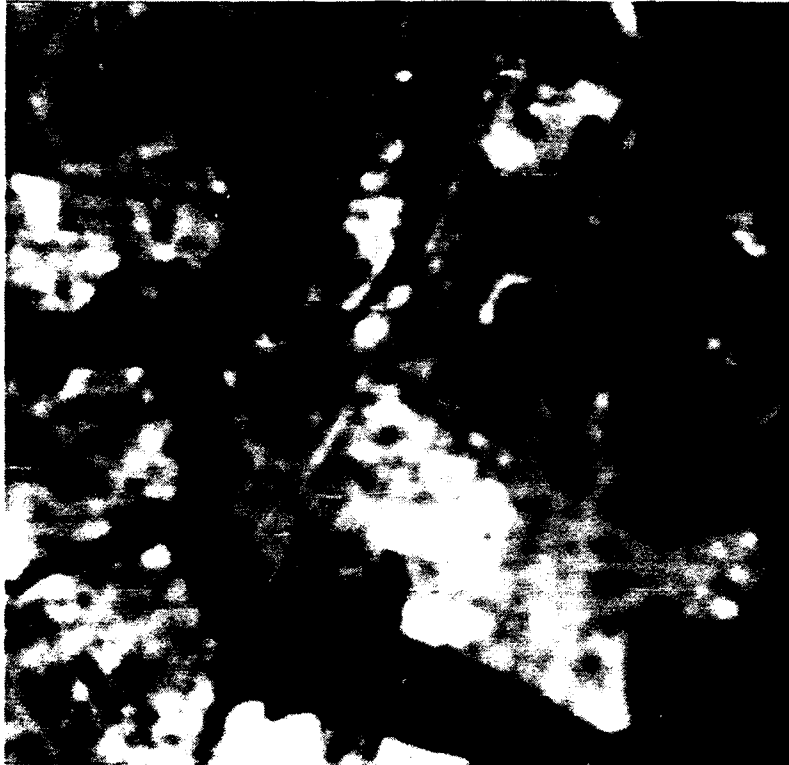
*Figure 30. Processed image for a signal-to-noise ratio of 10.*

46
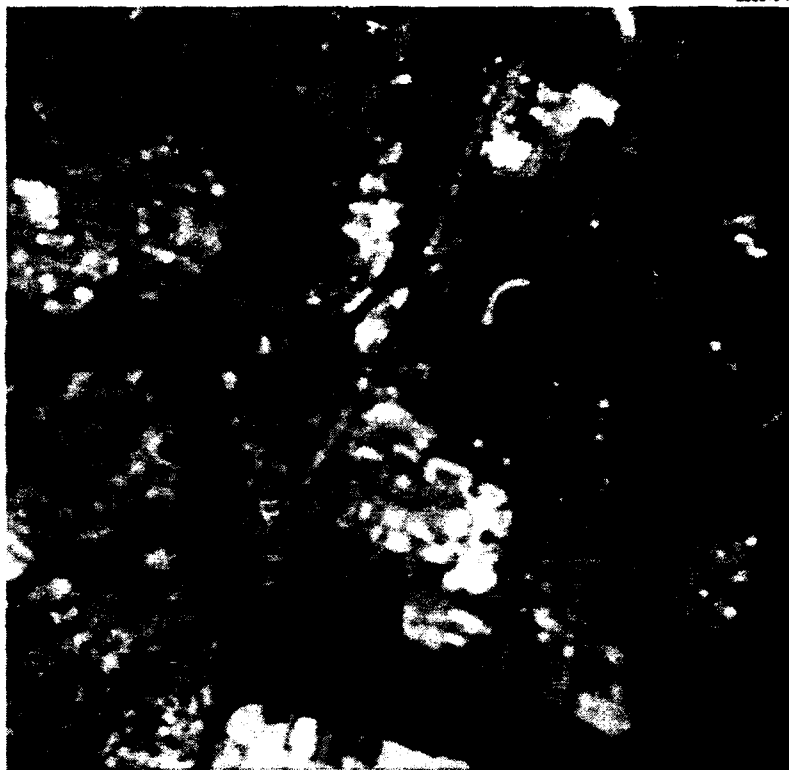
*Figure 31. Processed image for a signal-to-noise ratio of 100. This image is virtually indistinguishable from that obtained with a circular aperture.*

## 4.3 SIGNAL-TO-NOISE CALCULATIONS FOR A REPRESENTATIVE RECONNAISSANCE SCENARIO

The degree to which the recovery process can reproduce the full-aperture output is highly dependent on the signal-to-noise ratio achieved by the system. This point is perhaps best made by comparing the *MTF* functions for S/N ratios (in units of optical power) of 10, 30, and 100, as shown in Figure 32. The net system resolution is reduced by about a factor of 2 for a signal-to-noise ratio of 10; this number probably represents the lower limit of utility for this process. (In generating this plot a $\vartheta_\rho/\vartheta_{pix}$ ratio of 15 was assumed, which is consistent with a system having a 1-m ground resolution and a scene having a correlation length of 15 m [33].)

In view of this result, it would be useful at this point to perform a first-order calculation of the signal-to-noise ratio for a nominal set of viewing conditions. This computation requires the establishment of a number of new parameters, including the average source radiance, the radiance contrast, the sensor dwell time, sensor quantum efficiency, and the sensor noise level.
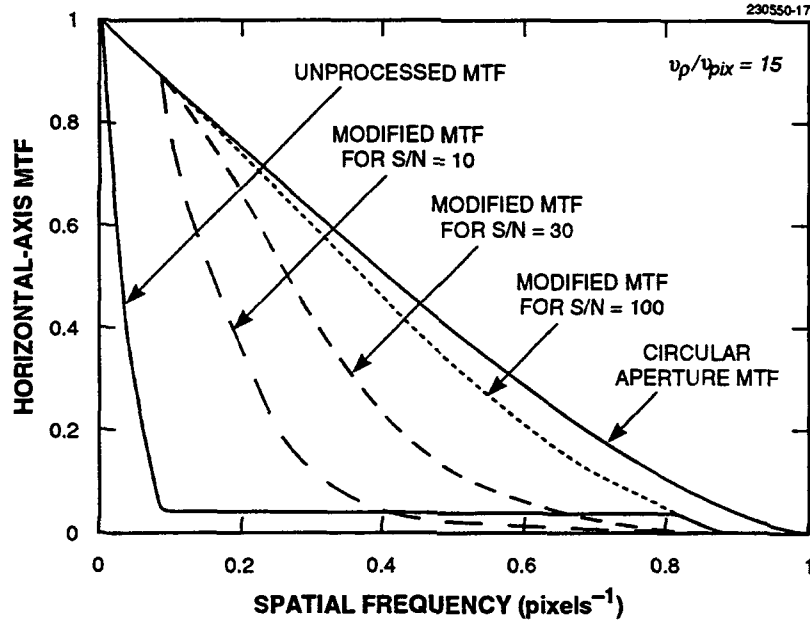
*Figure 32. Comparison of horizontal-axis MTFs for S/N ratios of 10 to 100. A resolution comparable to about one-half of the full aperture is achieved for S/N = 10.*

For an unresolved-target viewing scenario, illustrated in Figure 33, a square detector of dimension $d$ collects light originating from a ground patch of area $(d_{pix})^2 = (dR/f)^2$, where $D$ is the aperture diameter and $f$ is the telescope focal length. The collector subtends a solid angle equal to $(\pi/4)(D/R)^2$ with respect to the ground.
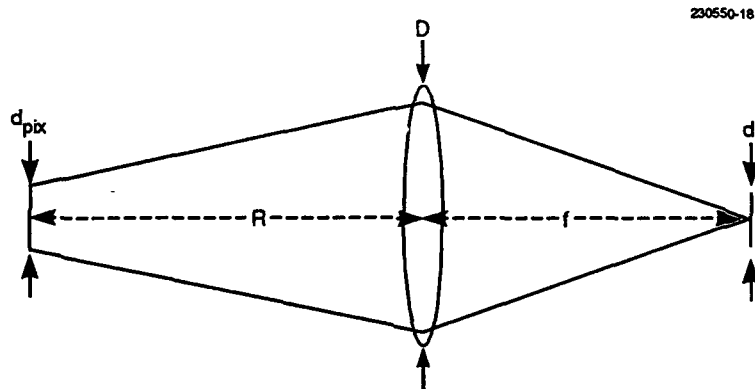


*Figure 33. Light-collection geometry for a telescope with a collection aperture, D, and focal length, f.*

48

This geometry results in the following expression for the number of electrons generated by the sensor within the spectral bandwidth $\lambda_1 < \lambda < \lambda_2$:

$$N_e = \underbrace{\frac{\pi d^2}{4(f/\#)^2}}_{\substack{\text{geometrical} \\ \text{factor}}} \int_{\lambda_1}^{\lambda_2} \left(\frac{\lambda}{hc}\right) \underbrace{\alpha \beta \tau_d \eta(\lambda)}_{\substack{\text{collection} \\ \text{efficiency}}} \underbrace{\varepsilon(\lambda) N(\lambda)}_{\substack{\text{source} \\ \text{spectral radiance}}} d\lambda \quad , \tag{32}$$

where the following definitions apply:

$d$ = detector size (m)
$f/\#$ = camera f/number
$\alpha$ = net system transmission
$\beta$ = telescope thinning factor
$\eta(\lambda)$ = detector quantum efficiency
$N(\lambda)$ = spectral radiance (W/m$^2$-sr-m)
$\varepsilon(\lambda)$ = source reflectivity (reflected solar radiation) or emissivity (blackbody radiation).

To satisfy the Nyquist criterion the detector size should be approximately equal to $f\lambda/2D$, in which case Equation (32) can be rewritten

$$N_e = \frac{\pi \alpha \beta \tau_d \lambda_c^2}{16} \int_{\lambda_1}^{\lambda_2} \left(\frac{\lambda}{hc}\right) \eta(\lambda)\, \varepsilon(\lambda) N(\lambda) d\lambda \quad , \tag{32.a}$$

where $\lambda_c$ is the center of the spectral bandwidth. For some missions it may be advantageous to intentionally degrade the sensor's resolution to increase the total field-of-view or reduce the data bandwidth. As a result, the dimensions of the pixel ground patch would establish the detector size, so that $d = d_{\text{pix}}/R$ and the following form will obtain

$$N_e = \frac{\pi \alpha \beta \tau_d d_{\text{pix}}^2 D^2}{4R^2} \int_{\lambda_1}^{\lambda_2} \left(\frac{\lambda}{hc}\right) \eta(\lambda)\, \varepsilon(\lambda) N(\lambda) d\lambda \quad . \tag{32.b}$$

Equation (32.a) is appropriate for high-altitude IR systems, whereas (32.b) is applicable for most low-altitude missions.

The dwell time of the system can be computed from the orbital period of the satellite. For a circular orbit [34]

$$T_o = 2\pi \sqrt{\frac{(R+R_e)^3}{GM_e}} \quad , \tag{33}$$

where

$G = 6.67 \times 10^{-11}$ nt-m$^2$/kg$^2$ is the gravitational constant

$M_e = 5.98 \times 10^{24}$ kg is the mass of the earth

$R_e = 6.36 \times 10^6$ m is the radius of the earth

$R$ = satellite altitude.

If the motion of the satellite is used to generate two-dimensional images in a "push broom" fashion, the pixels on the ground are scanned at a velocity of

$$v = \frac{2\pi R_e}{T_o} \quad . \tag{34}$$

It follows that the dwell time is equal to

$$\tau_d = n_d \frac{d_{pix}}{v} \quad , \tag{35}$$

where the parameter $n_d$ represents the number of pixels in the detector array along the direction of motion that are used for TDI (time delay and integration). For low-altitude satellites the orbital period is almost independent of the satellite altitude, in which case the dwell time is proportional to $R/D$.

At this point it is necessary to establish expressions for the spectral radiance. For blackbody radiation [35]

$$N(\lambda) = \frac{2hc^2}{\lambda^5 \{\exp(hc/\lambda kT) - 1\}} \quad , \tag{36}$$

where

$c$ = velocity of light = $3.00 \times 10^8$ m/s

$h$ = Planck's constant = $6.63 \times 10^{-34}$ W-s$^2$

$k$ = Boltzmann's constant = $1.38 \times 10^{-23}$ W-s/K

$T$ = source temperature $\approx 300$ K.

For most scenes the image contrast is driven primarily by temperature fluctuations in the local terrain. To a good approximation, the signal can be characterized as the product of the derivative of Equation (32.a) with respect to temperature and the scene standard deviation, $\sigma_T$:

50

$$\text{signal} = \frac{\partial N_e}{\partial T}\sigma_T = \frac{\pi\alpha\beta\tau_d\lambda_c^2\sigma_T}{16}\int_{\lambda_1}^{\lambda_2}\left(\frac{\lambda}{hc}\right)\eta(\lambda)\,\varepsilon(\lambda)\left[\frac{2h^2c^3\exp(hc/\lambda kT)}{kT^2\lambda^6\{\exp(hc/\lambda kT)-1\}^2}\right]d\lambda \quad . \tag{37}$$

The value of $\sigma_T$ is typically in the range $1°$ to $5°C$ [33].

The noise generated by the sensor includes several terms, the most important of which are quantum noise, $n_Q$, due to photon-arrival statistics; additive temporal noise, $n_{AT}$, which is primarily due to readout-amplifier fluctuations; and multiplicative fixed pattern noise, $n_{MFP}$ [36]. The magnitude of the first and third effect is dependent on the average number of collected electrons

$$n_Q = \sqrt{\overline{N}_e} \quad , \text{and} \tag{38}$$

$$n_{MFP} = U_c\,\overline{N}_e \quad , \tag{39}$$

where $U_c$ is the array uniformity following a two-point response correction. The total noise (standard deviation of the temporal and spatial fluctuations) is the square root of the sum of the variances

$$\text{noise} = \sqrt{n_Q^2 + n_{AT}^2 + n_{MFP}^2} = \sqrt{\overline{N}_e + n_{AT}^2 + U_c^2\,\overline{N}_e^2} \quad . \tag{40}$$

For a diffraction-limited IR system sampled at the Nyquist frequency, the average number of electrons collected by a pixel during a dwell time $\tau_d$ is

$$\overline{N}_e = \frac{\pi\alpha\beta\tau_d\lambda_c^2}{16}\int_{\lambda_1}^{\lambda_2}\left(\frac{\lambda}{hc}\right)\eta(\lambda)\,\varepsilon(\lambda)\left[\frac{2hc^2}{\lambda^5\{\exp(hc/\lambda kT)-1\}}\right]d\lambda \quad . \tag{41}$$

Nominal values for $\eta$, $n_{AT}$, and $U_c$ for large InSb arrays are 0.5, 250 rms electrons, and 1%, respectively.

For reflected solar radiation the expression is more complex because a number of additional parameters are involved, such as the angle between the sun and the normal to the earth's surface. To first order the source can be modeled as a 5900 K blackbody with an emissivity that incorporates all the geometrical factors involved in the reflection of light from the sun to the satellite. By comparing data given in the *Infrared Handbook* [37] with the output of a blackbody having unity emissivity, the following approximation is developed from Equations (32.b) and (36):

51

$$\overline{N}_e = \frac{\pi\alpha\beta\tau_d\, d_{\text{pix}}^2\, D^2}{4R^2} \int_{\lambda_1}^{\lambda_2} \left(\frac{\lambda}{hc}\right)\eta(\lambda)\left[3\text{x}10^{-6}\frac{2hc^2}{\lambda^5\{\exp(hc/\lambda kT)-1\}}\right]d\lambda \quad , \qquad (42)$$

where $T = 5900$ K. In this case the contrast is due to fractional changes in the terrain reflectivity, $\sigma_r$, which is perhaps of the order of 0.1. Thus the signal is expected to be

$$\text{signal} = \frac{\pi\alpha\beta\tau_d\, d_{\text{pix}}^2\, D^2\, \sigma_r}{4R^2} \int_{\lambda_1}^{\lambda_2} \left(\frac{\lambda}{hc}\right)\eta(\lambda)\left[3\text{x}10^{-6}\frac{2hc^2}{\lambda^5\{\exp(hc/\lambda kT)-1\}}\right]d\lambda \quad . \qquad (43)$$

The noise for this system is obtained by substituting Equation (42) into (40); nominal values for $\eta$, $n_{AT}$, and $U_c$ for large Si arrays are 0.8, 5 rms electrons, and 0.25%, respectively.

An estimate of the achievable signal-to-noise ratio for an 8-m thinned-aperture telescope placed in geosynchronous orbit is given in Table 1. In developing this chart the dwell times of the two sensors have been adjusted to achieve an acceptable signal-to-noise ratio, from which it can be seen that the stare time is dominated by the requirements of the visible system. It was discovered, however, that an S/N greater than 10 could not be achieved with the IR system, because its composite noise is dominated by detector nonuniformities at high signal levels.

The results of this calculation are positive in that signal-to-noise ratios of the order of 10 could be achieved with relatively modest dwell times. Although the evidence at this point is far from conclusive, there is reason to believe that the image restoration techniques described in this report can be successfully applied to large-aperture telescopes having fill factors as small as 10%.

## TABLE 1
### Parameter List For Baseline S/N Calculation

| Parameter | Symbol | Visible Sensor | IR Sensor |
|---|---|---|---|
| Detector Material | | Si | InSb |
| Center Wavelength | $\lambda_c$ | 0.6 μm | 4 μm |
| Satellite Altitude | $R$ | 1,000 km | 1,000 km |
| Aperture Diameter | $D$ | 10 m | 10 m |
| Detector Array Size | $n_d$ | 1024 x 1024 | 1024 x 1024 |
| System Transmission | $\alpha$ | 0.5 | 0.5 |
| Thinning Factor | $\beta$ | 0.1 | 0.1 |
| Quantum Efficiency | $\eta$ | 0.8 | 0.5 |
| Temporal Noise | $n_{AT}$ | 5 electrons | 250 electrons |
| Corrected Uniformity | $U_c$ | 0.25% | 1% |
| Pixel Dimension | $d_{pix}$ | 20 cm | 20 cm |
| Effective Dwell Time | $\tau_d$ | 32 msec | 32 msec |
| Correlation Length | $\rho$ | 2 m | 2 m |
| Ground Emissivity | $\varepsilon$ | ---- | 0.9 |
| rms Thermal Signal | $\sigma_T$ | ---- | 3 °C |
| rms Reflectivity Signal | $\sigma_r$ | 0.1 | ---- |
| Signal-to-Noise Ratio[†] | $S/N$ | 33 | 10 |

† Designates optical power ratio, equivalent to electrical voltage.

53

# 5. CONCLUSIONS

This report offers convincing evidence of the utility of Fourier deconvolution in extracting improved imagery from nonideal optical receivers. Although it is shown that the quality of the recovered data is ultimately limited by the cut-off frequency of the system's optical transfer function, highly-attenuated frequency components can usually be recovered as long as the SNR exceeds the gain required for restoration. These conditions are met for many scenarios of practical interest.

This computational technique has been successfully applied to images of celestial objects collected by a ground-based telescope and has also been incorporated into a reconnaissance simulation involving a thinned-aperture optical satellite having a 10% fill factor. For both applications, a significant improvement over the resolution of the raw data has been demonstrated. In particular, the results of the reconnaissance simulation lend strong support to the feasibility of constructing inexpensive, lightweight surveillance satellites employing folded-mirror architecture.

# APPENDIX—CHARACTERIZATION OF AN OPTICAL SYSTEM

To provide a framework for the computational techniques that are discussed in the main body of this report, this appendix offers an overview of the physics and mathematics that describe the formation of an image by an optical system. This discussion is largely based on two excellent texts by Goodman [33,34], and in keeping with his development of this problem, dependent variables and normalization parameters are explicitly included throughout this section.

## A.1 BASIC CONCEPTS

The single-element optical system shown in Figure A-1 incorporates all the spatial relationships essential to this discussion. The lens is placed at the origin of the coordinate system, and the object and image planes are located at $z = -R$ and $z = f$, respectively. It is assumed that $R$ is much longer than the Fresnel distance, $D^2/\lambda$, where $D$ and $\lambda$ represent the aperture diameter and optical wavelength, respectively.
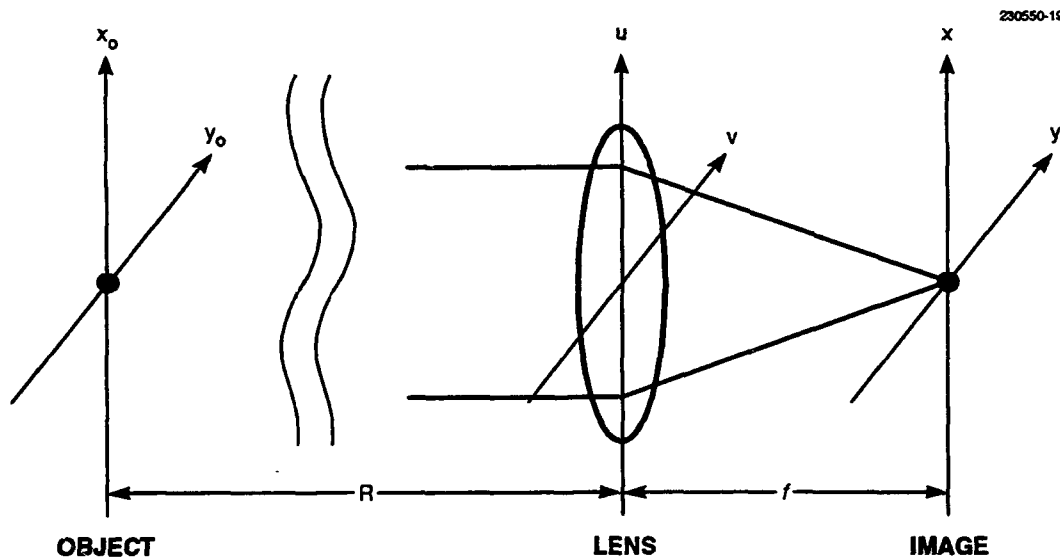


*Figure A-1. Spatial relationship between the object, pupil, and image planes of a simple imaging system. The object is assumed to be separated from the lens by a distance that is much larger than the Fresnel distance.*

57

For the geometry indicated, the lens is situated in the Fourier plane of both the object and the image. The electric field of radiation originating in the object plane is described by the complex function $U_o(x_o, y_o)$. In the plane of the lens the field is given by

$$U_l(u,v) = u_o\left(\frac{u}{\lambda R}, \frac{v}{\lambda R}\right) \ , \tag{A-1}$$

where

$$u_o(f_x, f_y) = \mathcal{F}\{U_o(x_o, y_o)\}$$

is the Fourier transform of $U_o(x_o, y_o)$. By applying a change of variables and the similarity theorem for Fourier transforms, Equation (A-1) may be rewritten as

$$U_l(u,v) = \frac{1}{(\lambda R)^2} \ \mathcal{F}\left\{U_o\left(\frac{x_o}{\lambda R}, \frac{y_o}{\lambda R}\right)\right\} \ . \tag{A-1.a}$$

When the object field is imaged by an ideal lens of infinite extent, the field in the image plane perfectly reproduces the object, albeit with a magnification factor of $M = f/R$ and an axis inversion

$$U_i(x,y) = \frac{1}{M} U_o\left(-\frac{x}{M}, -\frac{y}{M}\right) \ . \tag{A-2}$$

For a perfect optical system the electric fields in the lens and image planes are related by the expression

$$U_l(u,v) = \frac{1}{(\lambda f)^2} \ \mathcal{F}\left\{U_i\left(\frac{x}{\lambda f}, \frac{y}{\lambda f}\right)\right\} \ . \tag{A-3}$$

Any distortion of the field in the lens (or pupil) plane will introduce a corresponding distortion in the image plane. If the pupil function $P(u,v)$ is introduced, the field in the lens plane is modified in the following way:

$$U_l'(u,v) = P(u,v)\, U_l(u,v) \ . \tag{A-4}$$

The resulting image function can be expressed as either a convolution of the image-plane functions or the Fourier transform of the pupil-plane field

$$U_i'(x,y) = \frac{1}{(\lambda f)^2} \, \mathcal{F}^{-1}\left\{ U_i'\left(\frac{u}{\lambda f}, \frac{v}{\lambda f}\right)\right\} = U_i(x,y) \otimes \left[\frac{1}{(\lambda f)^2} \, \mathcal{F}^{-1}\left\{ P\left(\frac{u}{\lambda f}, \frac{v}{\lambda f}\right)\right\}\right] \quad \text{(A-5)}$$

For imaging-system applications the quantity of principal interest is the focal-plane intensity

$$I'(x,y) = \left| U_i'(x,y)\right|^2 . \quad \text{(A-6)}$$

When the illumination is incoherent, the intensity function is found to be the convolution of the ideal intensity $I(x,y) = \left| U_i(x,y)\right|^2$ and the squared modulus of the pupil-plane function transform

$$I'(x,y) = I(x,y) \otimes \left| \frac{1}{(\lambda f)^2} \, \mathcal{F}^{-1}\left\{ P\left(\frac{u}{\lambda f}, \frac{v}{\lambda f}\right)\right\}\right|^2 . \quad \text{(A-7)}$$

The second convolution term in Equation (A-7) is known as the point spread function (*PSF*), thus the more familiar form of this expression is

$$I'(x,y) = I(x,y) \otimes PSF(x,y) . \quad \text{(A-7.a)}$$

The effective point spread function of a complex optical system can be obtained by convolving the *PSFs* of the individual components or by performing the equivalent operation in Fourier space by taking the product of their Fourier transforms. The optical transfer function (*OTF*) is defined for this purpose as

$$OTF(f_x, f_y) = \frac{\displaystyle\int_{-\infty}^{\infty}\int_{-\infty}^{\infty} P(u,v)\, P^*\!\left(u - (\lambda f)\, f_x,\, v - (\lambda f)\, f_y\right) du\, dv}{\displaystyle\int_{-\infty}^{\infty}\int_{-\infty}^{\infty} |P(u,v)|^2 \, du\, dv} , \quad \text{(A-8)}$$

which is the autocorrelation of the pupil function with a unity normalization at the origin. The *OTF* is a complex Hermite function [i.e., *OTF(f) = OTF\*(-f)*] that describes both the intensity and phase of the frequency components of the electric field transmitted through the system. The modulus of this function is known as the modulation transfer function (*MTF*):

$$MTF(f_x, f_y) = \left| OTF(f_x, f_y)\right| , \quad \text{(A-9)}$$

which specifies the attenuation of the field intensity at a specified frequency. (The distinction between these two quantities is important in the discussion of speckle interferometry.) From Equations (A-7) and (A-8) it can be seen that the PSF and OTF are Fourier transform pairs:

$$PSF(x,y) = \frac{\mathcal{F}^{-1}\{OTF(f_x, f_y)\}}{\int\limits_{-\infty}^{\infty}\int\limits_{-\infty}^{\infty} \mathcal{F}^{-1}\{OTF(f_x, f_y)\}\, dx_i\, dy_i} \quad, \tag{A-10}$$

where the normalization applied here forces the two-dimensional integral to be one.

An example of the use of the $OTF$ to obtain a description of the far-field image is demonstrated for a perfect circular collector of diameter $D$. With this symmetry it is convenient to define the one-dimensional spatial frequency $f = \sqrt{f_x^2 + f_y^2}$, and the following expression obtains

$$OTF(f) = \begin{cases} \dfrac{2}{\pi}\left[\cos^{-1}\left(\dfrac{(\lambda f)|f|}{D}\right) - \dfrac{(\lambda f)|f|}{D}\sqrt{1 - \left(\dfrac{(\lambda f)|f|}{D}\right)^2}\right] & |f| \le D/\lambda f \\[2em] 0 & |f| > D/\lambda f \end{cases} \tag{A-11}$$

Notice that the cut-off frequency for a circular aperture is $f_o = D/\lambda f$, as illustrated in Figure A-2. The point spread function is computed using the Hankel transform; the result for a circular aperture is the familiar Airy pattern for the parameter $\rho = \sqrt{x^2 + y^2}$

$$PSF(\rho) = \left(\frac{\pi D^2}{4(\lambda f)^2}\right)\left[2\frac{J_1(\pi D\rho/\lambda f)}{\pi D\rho/\lambda f}\right]^2 \quad. \tag{A-12}$$

This function is shown in Figure A-3. The beamwidth (full width at half maximum) is approximately $\lambda f/D$.
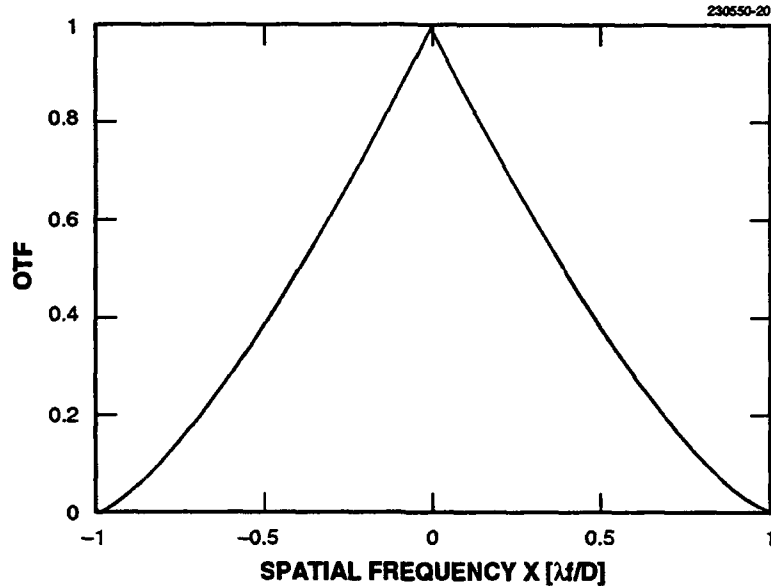
*Figure A-2.   Optical transfer function for a perfect circular aperture of diameter D.*

## A.2  IMAGE DEGRADATION DUE TO ATMOSPHERIC TURBULENCE

Any modification of the aperture function that results in a variation of the transmission or optical phase across the aperture will produce an *OTF* that is lower than the ideal function shown in Figure A-2.  The effect in the focal plane is to produce a beam that is broader than the diffraction-limited image plotted in Figure A-3.  For this reason the *OTF* has been used by lens designers to characterize static aberrations associated with optical systems.  This technique can also be applied to stochastic effects, such as those associated with atmospheric turbulence.

Following Goodman's approach, it is convenient to establish a new pupil function

$$P'(u,v) = P(u,v)\, t_s(u,v)  \; , \tag{A-13}$$

where $P(u,v)$ represents the aberration-free collector and $t_s(u,v)$ is the phase distortion function.

61
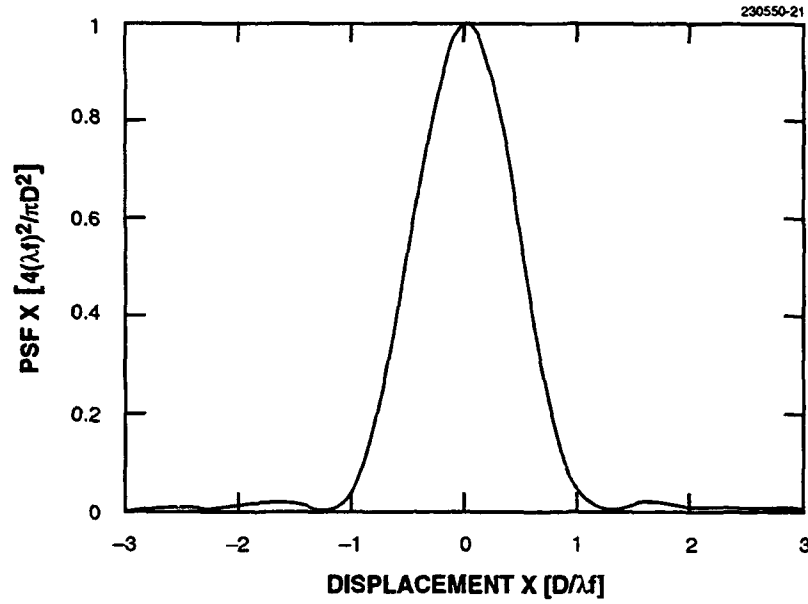
*Figure A-3. Point spread function for a perfect circular aperture of diameter D.*

The ensemble-average *OTF* is defined to be the ratio of the expectation values of the numerator and denominator of Equation (A-8):

$$OTF\left(f_x, f_y\right) = \frac{\int\limits_{-\infty}^{\infty} \int\limits_{-\infty}^{\infty} P(u,v) \, P^*\left(u - (\lambda f) f_x, v - (\lambda f) f_y\right) \left\langle t_s(u,v) \, t_s^*\left(u - (\lambda f) f_x, v - (\lambda f) f_y\right)\right\rangle du \, dv}{\int\limits_{-\infty}^{\infty} \int\limits_{-\infty}^{\infty} |P(u,v)|^2 \left\langle |t_s(u,v)|^2 \right\rangle du \, dv} .$$

(A-14)

If the phase distortion is the result of a stationary process, the order of integration can be interchanged so that

62

$$OTF(f_x, f_y) = \frac{\int\limits_{-\infty}^{\infty} \int\limits_{-\infty}^{\infty} P(u,v) P^*\left(u - (\lambda f) f_x, v - (\lambda f) f_y\right) du\, dv}{\int\limits_{-\infty}^{\infty} \int\limits_{-\infty}^{\infty} |P(u,v)|^2\, du\, dv}$$

$$\times \frac{\int\limits_{-\infty}^{\infty} \int\limits_{-\infty}^{\infty} \left\langle t_s(u,v) t_s^*\left(u - (\lambda f) f_x, v - (\lambda f) f_y\right)\right\rangle du\, dv}{\int\limits_{-\infty}^{\infty} \int\limits_{-\infty}^{\infty} \left\langle |t_s(u,v)|^2 \right\rangle du\, dv} \quad , \qquad \text{(A-15)}$$

which is the product of the aberration-free optical transfer function and the average phase-screen *OTF*. To simplify the notation to be used in the following discussion, we introduce the parameters $OTF_c$ and $\overline{OTF_t}$ to represent the diffraction-limited and turbulence *OTF*s, respectively. Thus, the previous equation can be rewritten

$$OTF(f_x, f_y) = OTF_c(f_x, f_y)\, \overline{OTF_t}(f_x, f_y) \quad . \qquad \text{(A-15.a)}$$

The expression for $OTF_c$ for a circular aperture was given in Equation (A-11).

A characterization of $\overline{OTF_t}$ in terms of well-established turbulence parameters is developed next. For phase-only perturbations the pupil-plane aberrations can be written as

$$t_s(u,v) = \exp[i\phi(u,v)] \quad , \qquad \text{(A-16)}$$

where $\phi(u,v)$ is a real phase function. From Equation (A-15) it can be seen that the average phase screen *OTF* is

$$\overline{OTF_t}(f_x, f_y) = \left\langle \exp\left[i\phi(u,v) - i\phi\left(u - (\lambda f) f_x, v - (\lambda f) f_y\right)\right]\right\rangle \quad . \qquad \text{(A-17)}$$

Since $\phi$ is assumed to be stationary, the random variable $\Delta\phi$ can be defined such that

$$\Delta\phi\left((\lambda f) f_x, (\lambda f) f_y\right) \equiv \phi(u,v) - \phi\left(u - (\lambda f) f_x, v - (\lambda f) f_y\right) \quad , \qquad \text{(A-18)}$$

which is independent of the spatial coordinates $u$ and $v$.

To carry this derivation further, it is necessary to assume a particular form for the phase probability density function. If $\phi$ is normally distributed with zero mean, then the probability density function for $\Delta\phi$ will also be Gaussian:

63

$$p_{\Delta\phi}(\omega) = \frac{1}{\sqrt{2\pi}\,\sigma_{\Delta\phi}} \exp\left(-\omega^2/2\sigma_{\Delta\phi}^2\right) \ . \tag{A-19}$$

The variance parameter $\sigma_{\Delta\phi}^2$ is a function of the separation distance between the two phase samples incorporated in Equation (A-18), and is seen to be equivalent to the structure function of $\phi$:

$$\sigma_{\Delta\phi}^2 = \overline{\left[\phi(u,v) - \phi\left(u - (\lambda f)\,\mathbf{f}_x,\, v - (\lambda f)\,\mathbf{f}_y\right)\right]^2} = D_\phi\left((\lambda f)\,\mathbf{f}_x,\,(\lambda f)\,\mathbf{f}_y\right) \ . \tag{A-20}$$

Insertion of Equation (A-19) into (A-17) gives the result

$$\overline{OTF_t}\left(\mathbf{f}_x, \mathbf{f}_y\right) = \int_{-\infty}^{\infty} \exp(i\omega)\,\frac{1}{\sqrt{2\pi}\,\sigma_{\Delta\phi}}\exp\left(-\omega^2/2\sigma_{\Delta\phi}^2\right)d\omega$$

$$= \exp\left(-\sigma_{\Delta\phi}^2/2\right) = \exp\left\{-\tfrac{1}{2}D_\phi\left((\lambda f)\,\mathbf{f}_x,\,(\lambda f)\,\mathbf{f}_y\right)\right\} \tag{A-21}$$

## A.2.1 Turbulence Effects on a Long-Exposure Image

The structure function for turbulence follows directly from Kolmogorov's [35] description of the power spectral density of the refractive index as a function of the wavenumber, $\kappa$,

$$\Phi_n(\kappa) = 0.033\,C_n^2\,\kappa^{-11/3} \ , \tag{A-22}$$

where $C_n^2$ is the structure constant. The structure constant is typically a function of position along the propagation path; the integrated turbulence strength $\mu_0$ has the following definition:

$$\mu_0 = \int_{\text{path}} C_n^2(z)\,dz \ . \tag{A-23}$$

The structure function that is derived from Equation (A-22) is

$$D_\phi(r) = 2.91\left(\frac{2\pi}{\lambda}\right)^2 \mu_0\, r^{5/3} = 6.88\left(r/r_o\right)^{5/3} \ . \tag{A-24}$$

64

The parameter, $r_o$, is the turbulence coherence length defined by Fried [36]:

$$r_o = \left\{ 0.423 \left( \frac{2\pi}{\lambda} \right)^2 \mu_0 \right\}^{-3/5} .$$

(A-25)

The average OTF for a propagation path characterized by the turbulence parameter, $r_o$, is

$$\overline{OTF_t}(f) = \exp\left\{ -3.44\left((\lambda f)f/r_o\right)^{5/3} \right\} .$$

(A-26)

This function is plotted in Figure A-4 along with the OTF for a circular aperture of diameter $r_o$. At this point the motivation for this definition of the turbulence coherence length becomes clear, because the two transfer functions are seen to be nearly identical at low spatial frequencies. The point spread function that develops from the application of the Hankel transform to Equation (A-26) has been derived by Sasiela [37]. The function is most easily expressed as a pair of asymptotic series that have different regions of validity:

$$\overline{PSF_t}(\rho) \approx \begin{cases} \left( \dfrac{\pi r_o^2}{4(\lambda f)^2} \right) \displaystyle\sum_{n=0}^{20} \dfrac{(-1)^n}{(n!)^2} \dfrac{\Gamma[6(n+1)/5]}{\Gamma[6/5]} \left[ \dfrac{1.495\, r_o}{\lambda f} \rho \right]^{2n} & : \rho \le 1.2\dfrac{\lambda f}{r_o} \\[20pt] \left( \dfrac{\pi r_o^2}{4(\lambda f)^2} \right) \displaystyle\sum_{n=0}^{2} \dfrac{(-1)^n}{n!} \dfrac{6\,\Gamma[(5n+6)/6]}{5\,\Gamma[6/5]\,\Gamma[-5n/6]} \left[ \dfrac{1.495\, r_o}{\lambda f} \rho \right]^{-(5n+6)/3} & : \rho > 1.2\dfrac{\lambda f}{r_o} \end{cases}$$

(A-27)

For first-order computations within two beam radii of the center, a Gaussian form can be substituted:

$$\overline{PSF_t}(\rho) \approx \left( \frac{\pi r_o^2}{4(\lambda f)^2} \right) \exp\left\{ -\left( \frac{\pi r_o}{2\lambda f} \rho \right)^2 \right\} .$$

(A-28)

As expected, the point spread function for uncorrected turbulence is very similar to the diffraction pattern generated by a circular aperture of diameter $r_o$. These two functions are compared in Figure A-5, along with the Gaussian approximation given in Equation (A-28). The Gaussian form significantly underestimates the beam intensity for large displacement values.

An approximation for the composite point spread function for the aperture and turbulence follows from the observation made in Figure A-4 that the OTF for a circular aperture is closely approximated by the function

$$OTF_c(f) = \exp\left\{ -3.44\left((\lambda f)f/D\right)^{5/3} \right\} .$$
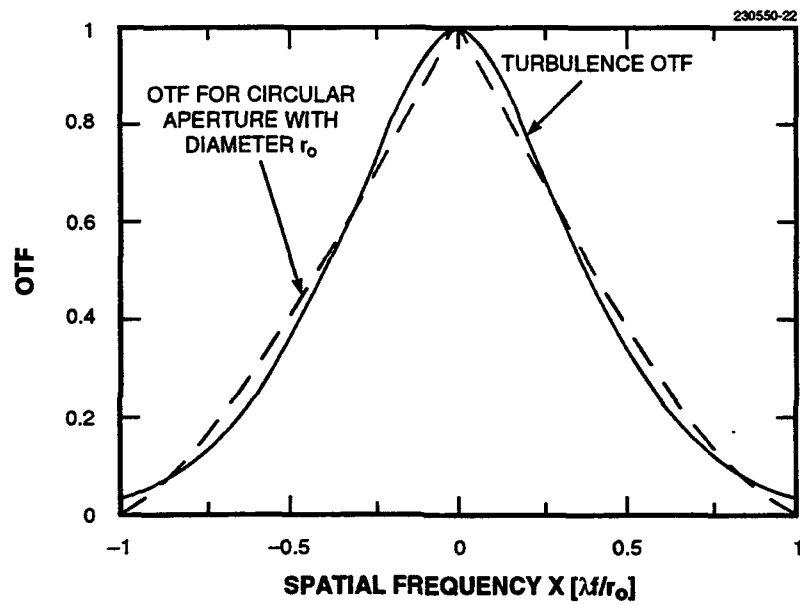
(A-29)

65

*Figure A-4. Comparison of the optical transfer functions for turbulence and a circular aperture of diameter $r_o$.*
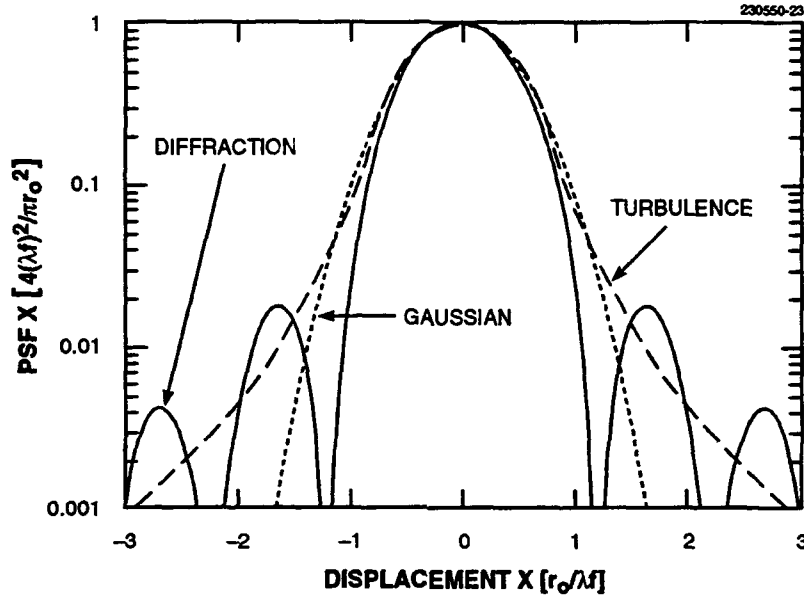
66

*Figure A-5. Comparison of the point spread functions for turbulence and a circular aperture of diameter $r_0$.*

The product of Equations (A-26) and (A-29) yields the result

$$\left[OTF(f)\right]_{\text{long exposure}} = OTF_c(f)\,\overline{OTF_t}(f) \approx \exp\left\{-3.44\left[(\lambda f/D)^{5/3} + (\lambda f/r_o)^{5/3}\right]f^{5/3}\right\} \quad \text{(A-30)}$$

If the same Gaussian-profile approximation developed in Equation (A-28) is applied to Equation (A-30), the following representation is obtained:

$$\left[PSF(\rho)\right]_{\text{long exposure}} \approx \left(\frac{\pi\,D_e^2}{4(\lambda f)^2}\right)\exp\left\{-\left(\frac{\pi\,D_e}{2\lambda f}\,\rho\right)^2\right\} , \quad \text{(A-31)}$$

where

$$D_e \equiv \left[D^{-5/3} + r_o^{-5/3}\right]^{-3/5} \quad \text{(A-32)}$$

67

represents the effective aperture diameter of the optical system and beam propagation path. The ratio of the on-axis beam intensity to the diffraction-limited value (Strehl ratio) is derived by taking the ratio of Equations (A-31) and (A-12) for $\rho = 0$:

$$[\text{Strehl}]_{\text{long exposure}} \approx \left\{ 1 + (D/r_o)^{5/3} \right\}^{-6/5} . \tag{A-33}$$

## A.2.2 Turbulence Effects on a Short-Exposure Image

When the exposure time is short compared to the atmospheric time constant (~ 1 ms), low spatial-frequency perturbations that introduce time-varying displacements of the beam centroid are eliminated; the same condition results when a tracking system is used for beam stabilization. If the assumption is made that the random variable associated with the centroid position has a Gaussian distribution that is statistically independent of any high spatial-frequency distortion effects, then the *OTF* of turbulence for short exposures is found to have the form [38]

$$\overline{OTF_t}(f) = \exp\left\{ -3.44((\lambda f)f/r_o)^{5/3} \left[ 1 - ((\lambda f)f/D)^{1/3} \right] \right\} . \tag{A-34}$$

Figure A-6 shows a plot of Equation (A-34) for the condition $D/r_o = 4$.

Although a rigorous expression for the short-exposure beam profile has not been derived (the application of Sasiela's technique is extremely difficult in this case), it has long been recognized that short-exposure beams have a diffraction-limited core that is surrounded by an extended halo. An approximate expression for the far-field point spread function can be developed by appropriately decomposing the short-exposure *OTF* into these two components. Because the screen *OTF* for an unperturbed field has a constant value of unity, it seems reasonable to define the constant part of $\overline{OTF_t}(f)$ to be the diffraction-limited component. Solving for the minimum value of Equation (A-34) results in

$$\left[ \overline{OTF_t}(f) \right]_{\text{diffraction-limited component}} = \exp\left\{ -0.23(D/r_o)^{5/3} \right\} \equiv S_o . \tag{A-35}$$

The *OTF* that describes the remaining energy is given by the difference between Equations (A-34) and (A-35). Since this function will later be multiplied by the aperture *OTF* (see Figure A-2) to obtain the final result, the high-frequency peak can be safely neglected. Following the procedure established earlier to obtain a Gaussian point spread function approximation, an exponential form is postulated for the turbulence-limited fraction of the short-exposure *OTF*:

$$\left[ \overline{OTF_t}(f) \right]_{\text{turbulence-limited component}} \approx [1 - S_o] \exp\left\{ -3.44((\lambda f)f/a)^{5/3} \right\} , \tag{A-36}$$

68

where the beam diameter $a$ is treated as a free parameter that is adjusted to obtain a best fit to the low-frequency peak. Maintaining a good fit over a wide range of $D/r_o$ values is not straightforward because one must take into account the subtraction of the constant, $S_o$, as well as the effects of the $(\lambda f/D)^{1/3}$ term in the exponent of Equation (A-34). A semi-empirical expression that appears to work well is

$$a \approx \frac{D}{\left\{ (D/r_o)^{5/3} - [1 - S_o](D/r_o)^{4/3} \right\}^{3/5}} \cdot \qquad \text{(A-37)}$$

Equations (A-35) and (A-36) are compared with the exact expression for the short-exposure turbulence $OTF$ in Figure A-6.

The net $OTF$ for the optical system and the propagation path is derived by multiplying the sum of the two turbulence components by the aperture $OTF$ given in Equation (A-29):

$$OTF(f) = OTF_c(f)\,\overline{OTF_t}(f)$$

$$\approx S_o\,\exp\left\{-3.44((\lambda f)f/D)^{5/3}\right\} + [1 - S_o]\,\exp\left\{-3.44\left[(\lambda f/D)^{5/3} + (\lambda f/a)^{5/3}\right]f^{5/3}\right\} . \quad \text{(A-38)}$$
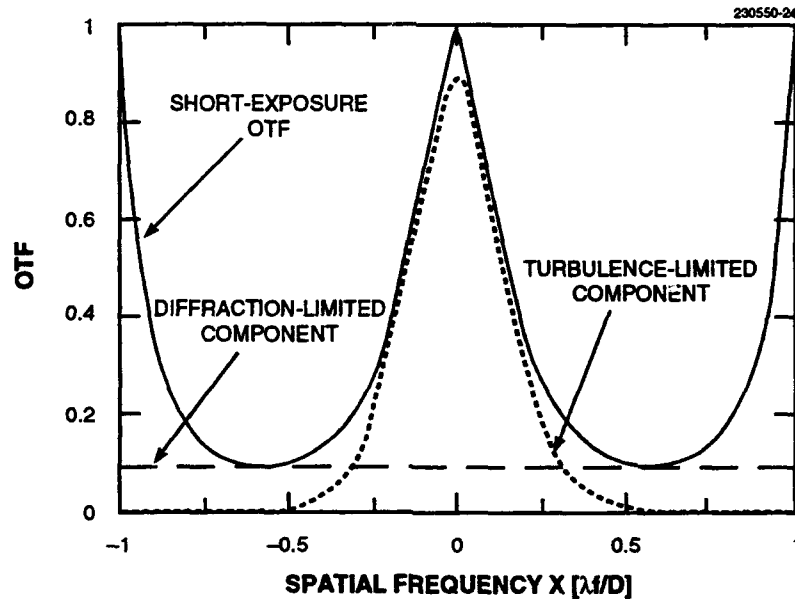


*Figure A-6.  Short-exposure optical transfer function for $D/r_o = 4$. To a good approximation, the low-frequency part of this function can be represented by the sum of a constant and an exponential curve that depends on the 5/3 power of the spatial frequency.*

The second term in this expression can be written more compactly by defining the effective aperture diameter

$$D_e \equiv \frac{D}{\left[1+(D/a)^{5/3}\right]^{3/5}} = \frac{D}{\left[1+(D/r_o)^{5/3}-[1-S_o](D/r_o)^{4/3}\right]^{3/5}} \ , \qquad \text{(A-39)}$$

which yields the result

$$\left[OTF(f)\right]_{\text{short exposure}} \approx S_o \ \exp\left\{-3.44((\lambda f)f/D)^{5/3}\right\} + [1-S_o] \exp\left\{-3.44((\lambda f)f/D_e)^{5/3}\right\} \ . \text{(A-38.a)}$$

From this form is developed a Gaussian approximation to the far-field point spread function following the arguments applied earlier in generating Equation (A-28):

$$\left[PSF(\rho)\right]_{\text{short exposure}} \approx S_o \left(\frac{\pi D^2}{4(\lambda f)^2}\right) \exp\left\{-\left(\frac{\pi D}{2\lambda f}\rho\right)^2\right\} + [1-S_o]\left(\frac{\pi D_e^2}{4(\lambda f)^2}\right) \exp\left\{-\left(\frac{\pi D_e}{2\lambda f}\rho\right)^2\right\} \ .$$

$$\text{(A-40)}$$

Figure A-7 presents a comparison of this approximation with the transform of Equation (A-34) for $D/r_o = 4$. The Strehl is obtained from the ratio of Equations (A-40) and (A-12) by setting $\rho$ to zero:

$$\left[\text{Strehl}\right]_{\text{short exposure}} \approx S_o + [1-S_o](D_e/D)^2 \ . \qquad \text{(A-41)}$$

The accuracy of this expression is better than 10% for $D/r_o$ values between 0.01 and 20.
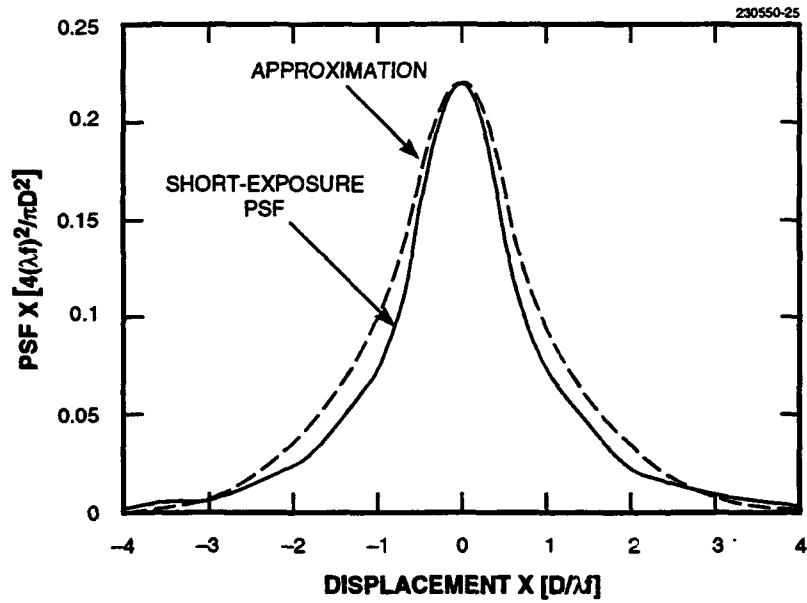
*Figure A-7.* Short-exposure point spread function for $D/r_o = 4$. The approximate form consists of a diffraction-limited central core and a halo with diameter $D_e$.

71

# REFERENCES

1. A. Labeyrie, "Attainment of diffraction limited resolution in large telescopes by Fourier analyzing speckle patterns in star images," *Astron. Astrophys.* **6**, 85–87 (1970).

2. D.Y. Gezari, A. Labeyrie, and R.V. Stachnik, "Speckle interferometry: Diffraction-limited measurements of nine stars with the 200-inch telescope," *Astrophys. J.* **173**, L1–L5 (1972).

3. D. Bonneau and A. Labeyrie, "Speckle interferometry: Color-dependent limb darkening evidenced on Alpha Orionis and Omicron Ceti," *Astrophys. J.* **181**, L1–L4 (1973).

4. A. Labeyrie, D. Bonneau, R.V. Stachnik, and D.Y. Gezari, "Speckle interferometry: III. High-resolution measurements of twelve close binary systems," *Astrophys. J.* **194**, L147–L151 (1974).

5. R. Nathan, "Digital video handling," Jet Propulsion Laboratory Technical Rep. 32-877 (5 January 1966).

6. C.W. Helstrom, "Image restoration by the method of least squares," *J. Opt. Soc. Am.* **57**, 297–303 (1967).

7. W.K. Pratt, *Digital Image Processing*, New York: John Wiley & Sons, Inc. (1978).

8. K.R. Castleman, *Digital Image Processing*, Englewood Cliffs, N.J.: Prentice-Hall (1979).

9. J.W. Hardy, "Adaptive optics—A progress review," *SPIE* **1542**, 2–17 (1991).

10. D.P. Greenwood and C.A. Primmerman, "Adaptive optics research at Lincoln Laboratory," *Linc. Lab. J.* **5**, 3–24 (1992).

11. J.M. Beckers, "Adaptive optics for astronomy: Principles, performance and applications," *Ann. Rev. Astron. Astrophys.* **31** (1993).

12. D.V. Murphy, "Atmospheric turbulence compensation experiments using cooperative beacons," *Linc. Lab. J.* **5**, 25–44 (1992).

13. B.R. Frieden, "Band-unlimited reconstruction of optical objects and spectra," *J. Opt. Soc. Am.* **57**, 1013–1019 (1967).

14. B.R. Frieden, "Restoring with maximum likelihood and entropy," *J. Opt. Soc. Am.* **62**, 511–518 (1972).

15. S.J. Wernecke and L.R. D'Addario, "Maximum entropy image reconstruction," *IEEE Trans. Comput.* **C-26**, 351–364 (1977).

16. U.J. Schwartz, "Mathematical-statistical description of the iterative beam removing technique (Method CLEAN)," *Astron. Astrophys.* **65**, 345–356 (1978).

17. J. Maeda, "Restoration of bandlimited images by an iterative damped least-squares method with adaptive regularization," *Appl. Opt.* **24**, 1421–1425 (1985).

18. C.A. Primmerman, D.V. Murphy, D.A. Page, and H.T. Barclay, "Compensation of atmospheric optical distortion using a synthetic beacon," *Nature* **353**, 141–143 (1991).

19. R.Q. Fugate, D.L. Fried, G.A. Ameer, B.R. Boeke, S.L. Browne, P.H. Roberts, R.E. Ruane, G.A. Tyler, and L.M. Wopat, "Measurement of atmospheric wavefront distortion using scattered light from a laser guide-star," *Nature* **353**, 144–146 (1991).

20. K.T. Knox and B.J. Thompson, "Recovery of images from atmospherically degraded short-exposure photographs," *Astrophys. J.* **193**, L45–L48 (1974).

21. C.R. Lynds, S.P. Worden, and J.W. Harvey, "Digital image reconstruction applied to Alpha Orionis," *Astrophys. J.* **207**, 174–180 (1976).

22. R.H.T. Bates and F.M. Cady, "Towards true imaging by wideband speckle interferometry," *Opt. Commun.* **3** (1980).

23. W I. Beavers, D.E. Dudgeon, J.W. Beletic, and M.T. Lane, "Speckle imaging through the atmosphere," *Linc. Lab. J.* **2** (1989).

24. ʻʒ. Rousset, J. Primot, and J.C. Fontanella, "Turbulent wavefront sensing and image processing," SPIE 88 Technical Symposium Southeast on Optics, Electro-Optics and Sensors (4–8 April 1988).

25. J. Primot, G. Rousset, and J.C. Fontanella, "Image deconvolution from wavefront sensing: Atmospheric turbulence simulation cell results," European Southern Observatory Conference on Very Large Telescopes and Their Instrumentation (21–24 March 1988).

26. R.C. Brown, *Introduction to Random Signal Analysis and Kalman Filtering*, New York: John Wiley & Sons, Inc. (1983).

27. J.D. Gonglewski, D.G. Voelz, J.S. Fender, D.C. Dayton, B.K. Spielbusch, and R.E. Pierson, "First astronomical application of postdetection turbulence compensation: Images of α Aurigae, ν Ursae Majoris, and α Geminorum using self-referenced speckle holography," *Appl. Opt.*, **29**, 4527–4529 (1990).

28. R.R. Parenti, "Adaptive optics for astronomy," *Linc. Lab. J.* **5**, 93–114 (1992).

29. R.R. Parenti and R.J. Sasiela, "SWAT system performance predictions," Lexington, Mass.: MIT Lincoln Laboratory, Project Rep. SWP-8, Revision 1 (10 March 1993).

30. J.C. Dainty and A.H. Greenaway, "Estimation of spatial power spectra in speckle interferometry," *J. Opt. Soc. Am.* **69**, 786–790 (1979).

31. J.W. Beletic, "Speckle imaging of complicated objects," Ph.D. thesis, Cambridge, Mass.: Harvard University (1989).

32. W.K. Pratt, *Digital Image Processing,* New York: John Wiley & Sons, Inc. (1978).

33. J.J. Otazo, E.W. Tung, and R.R. Parenti, "Digital filters for infrared target acquisition sensors," SPIE, **238**, 78–90 (1980).

34. D. Halliday and R. Resnick, *Physics for Students of Science and Engineering*, New York: John Wiley & Sons, Inc. (1965).

35. R.D. Hudson, Jr., *Infrared System Engineering*, New York: John Wiley & Sons, Inc. (1969).

36. M.J. Cantella, "Staring Sensor Systems," Lincoln Laboratory Project Memorandum No. 96PM-0002 (23 September 1992).

37. W.L. Wolfe and G.Z. Zissis, eds., *The Infrared Handbook*, Environmental Research Institute of Michigan (1978).

38. W. Goodman, *Introduction to Fourier Optics*, New York: McGraw-Hill Book Co. (1968).

39. W. Goodman, *Statistical Optics,* New York: John Wiley & Sons, Inc. (1985).

40. A. Kolmogorov, "The local structure of turbulence in incompressible viscous fluid for very large Reynolds' numbers," in *Turbulence, Classic Papers on Statistical Theory*, S.K. Friedlander and L. Topper, eds., Interscience Publishers (1961), pp. 151–155.

41. D.L. Fried, "Limiting resolution looking down through the atmosphere," *J. Opt. Soc. Am.* **56**, 1380–1384 (1966).

42. R.J. Sasiela, "A unified approach to electromagnetic wave propagation in turbulence and the evaluation of multiparameter integrals," Lexington, Mass.: MIT Lincoln Laboratory Technical Rep. No. 807 (1 July 1988). DTIC AD-A198062.

43. R.E. Hufnagel, "Propagation through atmospheric turbulence," in *The Infrared Handbook*, W.L. Wolfe and G.J. Zissis, eds., Environmental Research Institute of Michigan (1978), 6-26–6-32.

# REPORT DOCUMENTATION PAGE

| 1. AGENCY USE ONLY (*Leave blank*) | 2. REPORT DATE<br>1 June 1994 | 3. REPORT TYPE AND DATES COVERED<br>Technical Report |
|---|---|---|

**4. TITLE AND SUBTITLE**

Application of Fourier-Space Image-Restoration Techniques to Turbulence Compensation and Sparse-Aperture Imaging

**6. AUTHOR(S)**

Ronald R. Parenti

**5. FUNDING NUMBERS**

C — F19628-90-C-0002
PE — 63217C
PR — 33

**7. PERFORMING ORGANIZATION NAME(S) AND ADDRESS(ES)**

Lincoln Laboratory, MIT
P.O. Box 73
Lexington, MA 02173-9108

**8. PERFORMING ORGANIZATION REPORT NUMBER**

TR-996

**9. SPONSORING/MONITORING AGENCY NAME(S) AND ADDRESS(ES)**

Phillips Laboratory
U.S. Air Force ESC
Hanscom AFB
Bedford, MA 01730

**10. SPONSORING/MONITORING AGENCY REPORT NUMBER**

ESC-TR-93-347

**11. SUPPLEMENTARY NOTES**

None

**12a. DISTRIBUTION/AVAILABILITY STATEMENT**

Approved for public release; distribution is unlimited.

**12b. DISTRIBUTION CODE**

**13. ABSTRACT** (*Maximum 200 words*)

Image reconstruction is important in any application in which the sensing apparatus or the intervening medium significantly corrupts the recorded data. Deconvolution processes are the oldest and best understood, and for many practical problems Fourier domain deconvolution is the method of choice because acceptable results can usually be obtained with a minimum of computational effort. This report describes two practical applications of the Fourier deconvolution process in which detailed knowledge of the system's instantaneous optical transfer function is effectively utilized. In the first example, speckle imagery is combined with wavefront-sensor data to produce diffraction-limited images of celestial objects; the results are shown to compare favorably with the output of a fully operational adaptive optics system. The second application involves a sparse-aperture collection system that could be incorporated into a lightweight space telescope; this discussion includes an assessment of the practical utility of sparse-aperture receivers in a realistic signal-to-noise environment.

**14. SUBJECT TERMS**

| Fourier deconvolution | turbulence compensation |
|---|---|
| adaptive optics | sparse-aperture imaging |
| speckle interferometry | Landsat image processing |

**15. NUMBER OF PAGES**
88

**16. PRICE CODE**

| 17. SECURITY CLASSIFICATION OF REPORT<br>Unclassified | 18. SECURITY CLASSIFICATION OF THIS PAGE<br>Unclassified | 19. SECURITY CLASSIFICATION OF ABSTRACT<br>Unclassified | 20. LIMITATION OF ABSTRACT<br>Same as Report |
|---|---|---|---|